Structural Health Monitoring of Aircraft Structures

B. Rocha[1], C. Silva[2], C. Keulen[3], M. Yildiz[4], and A. Suleman[3*]

[1] Instituto Superior Tecnico, Lisbon, Portugal
[2] Portuguese Air Force Academy, Sintra, Portugal
[3] University of Victoria, Victoria, BC, Canada
[4] Sabanci University, Istanbul, Turkey

1 Introduction

Aircraft structures operate in harsh conditions sustaining high loads, fatigue cycles and extreme temperature variations. Therefore, inspections to assess the structural condition is of the utmost importance for safe and efficient operation of aircraft. Also, to achieve lighter structures, damages are allowed to exist in aircraft during operation as long as they are within predetermined and safe limits. Thus, aircraft structures are designed according to a damage tolerance philosophy.

Non-destructive testing and evaluation techniques developed in the last few decades and currently in application to assess the health of aircraft structures in operation, fail to detect localized damage, i.e. they are able to detect damage uniquely in limited areas in the vicinity of the inspection region. To obtain a full inspection, repetitive execution of these techniques in different areas of the structure requiring direct access is necessary. This involves complicated, time consuming and consequently expensive operations; particularly disassembly and re-assembly procedures that force aircraft to be grounded. When an aircraft is grounded and not in operation it is not profitable and represents an added cost for the operator (maintenance, hangar time, leasing, etc). Thus, structural inspections and maintenance are performed on a scheduled basis with increasing pressure from aircraft fleet operators to reduce inspection and maintenance time and extend intervals in between consecutive interventions. This increases the risk of damage

[*] Principal Investigator, IDMEC-IST, Lisbon, Portugal

W. Ostachowicz, J. Güemes (Eds.), *New Trends in Structural Health Monitoring*,
CISM International Centre for Mechanical Sciences, DOI 10.1007/978-3-7091-1390-5_2,

existence and growth between inspections. Damage might also exist and grow in regions not inspected. All of these issues point to a need for a reliable, persistent and integrated real time and global structural integrity evaluation system.

In the early years of aviation (1920-1940), structures were designed according to the Infinite Life concept, where they would be operated below their fatigue stress limit. Obviously the application of such a concept in design resulted in very heavy structures thus limiting aircraft performance. It is noted that increasing aircraft weight must be counterbalanced by increasing generated lift, leading to an increase in either wing area, or wing loading, and consequently increasing structural weight. Increasing lift generation also increases drag generation that in turn must be counterbalanced by increasing thrust. This requires the use of powerful and likley larger and heavier powerplants, with increased fuel consumption, leading again to the increase of overall weight. Moreover, higher structural weight for a certain lift generated decreases the available payload weight (both passenger and cargo capacity), maneuvering capabilities and aircraft performance such as endurance and range, since available fuel weight is reduced.

To overcome these chellenges a Safe Life structural design and operation approach was then adopted. In this concept, a finite service life was established, within which the probability of fatigue cracks to initiate and develop was extremely remote. The derivation process to determine structural life span was therefore based on the crack initiation stage of the fatigue failure process. This concept was applied in structural design during several years. However, it did not account for flaws generated in manufacture or other forms of damage that reduce structural life, such as corrosion or accidental damage. Damage models and stress analysis were also often inaccurate and inadequate. These inaccuracies have led to multiple accidents, like those of the five DeHavilland COMET, between May 1952 and January 1954. In the last accident, the aircraft had only about 1000 flights, while its flight simulation tests predicted an operational life of 3060 flights. Additionally, in the Safe Life concept, the detection of defects in one component was automatically a cause for its removal from service. In the early seventies, the development of inspection technology, in particular the ability to detect smaller flaws, led to an increasing number of parts being rejected. At that time, advances in the discipline of fracture mechanics enabled the prediction of whether a crack of a given size would induce the failure of a component under a particular load if particular material properties and fracture resistance were known. Models were developed to predict the growth rate of cracks subject to cyclic loads (fatigue). It became possible to have structures in service with existing defects as long as their existence and dimen-

sions were known and smaller than calculated maximum damage dimensions determined to lead to structural collapse.

A Fail Safe structural design and operation concept was then introduced in which a structure is designed to be capable of retaining required residual strength for a period of unrepaired service after sustaining a failure or partial failure of a primary structural element. Structures designed according to this concept present multiple load paths and use crack stoppers, so that stress levels after crack initiation are kept low providing controlled and slow crack growth rates. Simultaneously, structural design is performed to assure a high probability of crack detection before strength is reduced below limit load capabilities. The Fail Safe structural design and life concept evolved to the currently used Damage Tolerance philosophy. In this concept, worst case scenario assumptions of initial manufacturing defects are considered. Also details on sensitivity of inspection techniques (minimum detectable damage dimensions and other limitations imposed by the structures geometry, potential locations and characteristics of damages to detect, their orientation, etc), to be applied for in service crack detection, are accounted for. A service life before next inspection and structural repair is then predicted, based on quantitative calculations of crack growth rates and predicted flight loads severity. A regime of repeated inspections is defined to ensure a high probability of crack detection prior to catastrophic failure, i.e., a scheduled based inspection and maintenance is established (DOD, 1987).

2 Structural Health Monitoring Architectures

Two main transducer architecture strategies based on Lamb-wave propagation were implemented and evaluated, namely piezo networks and phased arrays. Optimum solutions with a minimum number of transducer are sought. The design variables range from sensor type, position, distances between sensors, and damage search area. In both architectures, wave emission and sensing based methods rely on the assumption that a discontinuity such as damage will produce an extra reflection, such as an echo. Figure 1 shows the echo received by a sensor after having produced a pulse. Based on the propagation velocity and time of flight it is possible to determine the distance between the echo generator and the sensor. With this information, one can determine a region where the damage may be present.

In order to detect the damage location with a network of sensors, a minimum of three transducers are required. If each transducer discloses a region of possible damage there will be a single point where the three regions intersect. This is the location of the damage. This technique is called triangulation. For phased arrays, the wave front propagation direction is

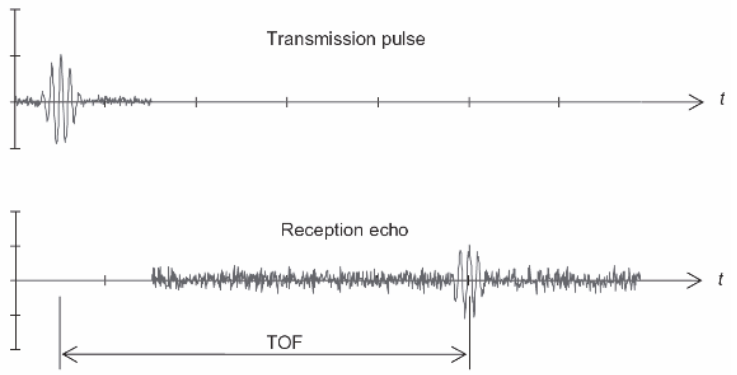

Figure 1. ToF echo detection

predetermined when the array is activated. Knowing the direction and the echo time of travel, it is possible to determine the damage location. The algorithm necessary to carry out this task depends on the approach selected. Network and phased array techniques rely on different algorithms but each can be based on the following principles. One principle involves executing a simple wave sweep. In this case, the damage presence results in the generation of unexpected reflections. The echo and permanent reflections created by the boundaries, other sensors, other wave types and discontinuities of the specimen being tested are sensed simultaneously. The second principle requires a comparison between the response from a damaged structure to an undamaged structure. The undamaged response, acting as a baseline is subtracted from the damaged response; the differences between the two responses indicate a change from the undamaged state. This approach allows for the isolation of the damage reflection eliminating the permanent reflections. Despite the higher complexity associated with the second approach due to the requirement of storing the undamaged response at all times, it does ease the damage detection. On one hand, the problem of having a superposition of permanent reflections along with damage is ruled out. On the other hand, the specimen deterioration, for example by aging, can result in various non-damage related patterns.

2.1 Sensors Network Architecture

The sensors network consists of an architecture where the piezo sensors are distributed in a pre-determined form on the thin structure. Two different

damage detection techniques can be implemented for the network approach. A direct technique that uses all of the transducers as both actuators and sensors, and a second, more complex method that uses one transducer as both sensor and actuator and the remaining as only sensors. Figure 2 shows both methods, with dots representing the transducer location.

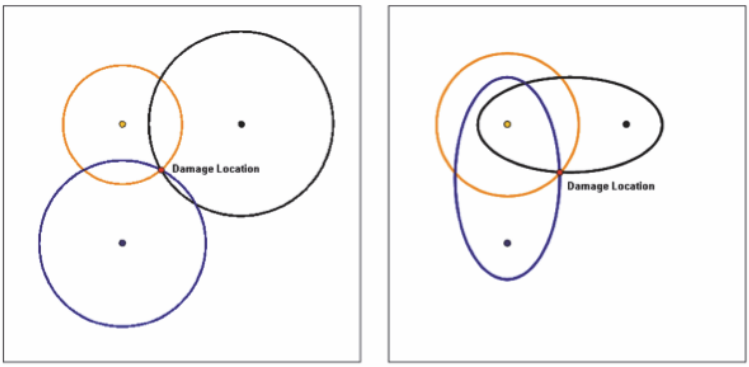

Figure 2. Regions of possible damage and damage location for a three sensor network

Using the first technique, assuming that the propagation velocity is equal in every direction, three circles indicating the location of an echo can be determined (shown on the left of Figure 2). The circles result from the fact that echoes and generated waves travel on the same path but in opposite directions. With the second technique, one circle and two ellipses are calculated (shown on the right). The circle is applied around the actuator transducer. The response gathered by the sensor transducers will receive an echo created by the damage. The time at which this echo is sensed will result from the summation of two different distances. The first will correspond to the distance travelled by the generated wave until it reaches the damage. The second will be the one travelled by the echo between the damage and the sensor. The geometric figure that matches this characteristic is an ellipse since the sum of the distances from any point of the ellipse to the actuator and sensor remains constant. For the first case presented, knowing the wave propagation speed and the time spent between its emission and echo detection, the travelled distance can be calculated. This principle looks at each piezo as both actuator and sensor. The algorithm consists of these steps:

1. An actuation frequency is selected and the wave propagation speed V

in the material is determined by simulation of experimentation.
2. Separate tests are performed using each actuator individually.
3. The sensed response gathered by only the actuator transducer is recorded.
4. Step 2 is repeated on the damaged structure.
5. Step 3 is repeated. At this point responses for both undamaged and damage profiles are obtained.
6. For each pair of data, the time t_i, at which the echo occurred (i is the transducer number) is determined.
7. Knowing the travel speed and the time the radial distance to the damage (r_i) can be determined. The travelled distance will correspond to two times the radius as in (1):

$$2r_i = Vt_i \tag{1}$$

8. For each transducer a circle using the transducer centre position (x_i, y_i) and the distance found on Step 7 as radius r_i is defined:

$$(x - x_i)^2 + (y - y_i)^2 = r_i^2 \tag{2}$$

9. The system of three equations for the unknown coordinates (x, y) can now be solved. They correspond to the damage position.

This approach does not take advantage of the presence of the other two transducers during Step 2. In order to use them, another assumption must be considered. Assuming that the damage acts as a source of reflections, besides the one that is sent to the actuator, others are sent in the remaining directions. Based on this and knowing the wave's propagation speed and the time spent between its emission and reflection detection, the travelled distance can be calculated. This principle looks at each transducer as a sensor. The algorithm follows the next steps for each test using just one actuation, the second technique described above:

1. An actuation frequency is selected and the wave propagation speed (V) in the material is determined by simulation or experimentation.
2. A single test is performed using just one transducer as an actuator.
3. The sensed response gathered by all transducers is recorded.
4. Step 2 is repeated on the damaged structure.
5. Step 3 is repeated. At this point responses for both undamaged and damage profiles are obtained.
6. For each pair of data, the time, t_{ij} at which the echo occurred (i is the actuator number, j is the sensor number) is determined.

7. Knowing the travel speed and the time, the distance travelled by the wave, d_i can be determined. This distance is the sum of the two, the first is the trip between the actuator and damage and the second is the trip between the damage and sensor:

$$d_{ij} = Vt_{ij} \tag{3}$$

8. For each transducer an ellipse can be defined. The actuator/sensor transducer positions are the two foci. The centre (h, k), semi-major axis a, distance between the two foci c, and semi-minor axis b can be calculated as follows (Important notes: x axis is parallel to the major axes and one ellipse will be in fact a circle, which corresponds to the actuator PZT).

$$a_{ij} = \frac{d_{ij}}{2} \tag{4}$$

$$c_{ij} = \frac{\sqrt{(x_i - x_j)^2} + \sqrt{(y_i - y_j)^2}}{2} \tag{5}$$

$$b_{ij} = \sqrt{a_{ij}^2 - c_{ij}^2} \tag{6}$$

$$h'_{ij} = x_i + \frac{(x_j - x_i)}{2} \tag{7}$$

$$k'_{ij} = y_i + \frac{(y_j - y_i)}{2} \tag{8}$$

$$\frac{(x' - h'_{ij})^2}{a_{ij}^2} + \frac{(y' - k'_{ij})^2}{b_{ij}^2} = 1 \tag{9}$$

9. A common coordinate system is selected and the coordinates x', y', h' and k' are rotated in order to get x, y, h and k
10. The system of three equations (two ellipses and one circle) for the unknown coordinates (x, y) can now be solved. They correspond to the damage position.

Despite the increased complexity the latter algorithm provides extra data per test run.

2.2 Phased Arrays Architecture

To implement phased arrays, a number of PZTs must be actuated in a predetermined and synchronous way. The lag between each individual actuation determines the travel direction of the generated wave front. These lags are predetermined by the actuation system, which also sets the actuation

frequency and consequently, wave propagation velocity (V). Nevertheless, these lags are calculated using the acquired data. The orientation is determined by the lags. Consider that the array reference position is (x_A, y_A). Figure 3 describes the algorithm. The red line shows the admissible damage locations, blue lines represent the wave front positioning at two different time instances, orange lines represent the wave front boundaries, (d_{WF} is the distance travelled by the wave front, d_R is the distance travelled by the echo produced by the damage, d_E is the length of the line that completes the right triangle created by d_{WF} and d_R.

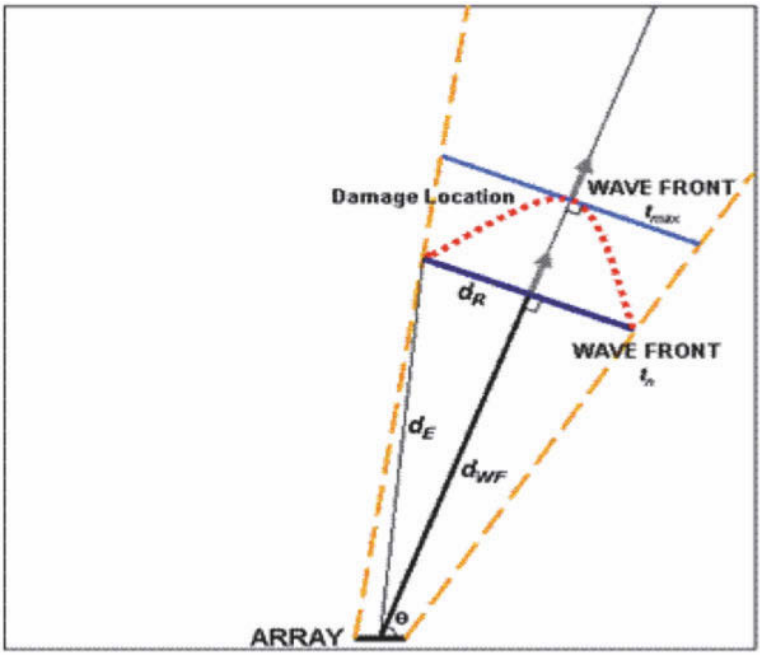

Figure 3. Damage location for a linear phased array

For the previously defined orientation, the algorithm follows these steps:

1. One test is run using the phased array.
2. The sensed response gathered by all array transducers is stored.
3. Step 1 is repeated on the damaged structure.
4. For each transducer, the undamaged data is subtracted from the damaged data and the time at which the echo occurred, t_i (i = transducer number) is determined. This time corresponds to the time required

for the wave front to reach the defect added to the time spent by the reflection to reach the transducer.

5. Since the travel velocity (V_i) and the time (t_i) is known, the total distance (d_i) resulting from the one travelled by the wave front (d_{WF}) added to the echo one (d_E) can be determined for each transducer:

$$d_i = Vt_i \tag{10}$$

$$d_i = d_{WF} + d_E = Vt_i \tag{11}$$

6. Note that the line established by the damage and the array may not correspond to the wave front propagation line direction. In order to determine the damage position, an iterative calculation must be made.
7. The wave front travelled distance at each time.

$$d_{WF} = Vt_{WF},\ \ldots\ t_{WF} = 0\ \ldots\ t_{max} \tag{12}$$

Where t_{max} corresponds to the condition where the line, established by the damage and the array orientation equals the wave front propagation direction. In this particular situation:

$$d_{WF} = d_E \tag{13}$$

8. For generic conditions, first the echo travelled distance, resulting from the subtraction between the total distance and travelled wave front distance has to be determined iteratively:

$$d_E = d_i - d_{WF} \tag{14}$$

9. For each time, the coordinates (x_{WF}, y_{WF}) corresponding to point at which the wave front is intersected by the line having the wave front propagation orientation is calculated:

$$x_{WF} = x_A + d_{WF}cos(\theta) \tag{15}$$

$$y_{WF} = y_A + d_{WF}sin(\theta) \tag{16}$$

10. Considering the right triangle constituted by d_{WF}, d_E and d_R one can calculate d_R. This distance is necessary to determine the two possible damage locations at each time instance:

$$d_R = \sqrt{d_{WF}^2} + d_E^2 \tag{17}$$

11. With this distance calculated, one can determine the two locations. Consider a left and a right point, with respect to (x_{WF}, y_{WF}):

$$x_{LEFT} = x_{WF} - d_R cos(\theta - \frac{\pi}{2}) \tag{18}$$

$$y_{LEFT} = y_{WF} - d_R sin(\theta - \frac{\pi}{2}) \tag{19}$$

$$x_{RIGHT} = x_{WF} + d_R cos(\theta - \frac{\pi}{2}) \tag{20}$$

$$y_{RIGHT} = y_{WF} + d_R sin(\theta - \frac{\pi}{2}) \tag{21}$$

The algorithm determines the probable damage location region for a given wave front orientation and echo detection. There will be as many regions as the number of transducers constituting the array. The network and phased array architectures presented are valid for constant thickness specimens made of isotropic materials. Only for these particular cases, wave propagation velocity can be considered constant. For anisotropic materials or thickness changing specimens, the velocity will not remain constant.

3 Piezoelectric Networks

In SHM experiments, with the transducer network setup defined, for each (and all) reference (considered undamaged) condition and for the actual (potential damaged) condition, each transducer in the network is actuated at a time, each actuation corresponding to one scan. The maximum amplitude of the actuation signal was established by the maximum amplitude enabled by the signal generation equipment ($\pm 15V$, for the NI PXI-5421). The frequency of actuation applied was of $340kHz$, according to what was established using the dispersion curves calculated for the aluminum plate (and its thickness of $2mm$); and for the PZT disc diameter selected to be $8mm$ - corresponding to an enhancement of actuation and sensing of the S_0 wave mode with a wavelength of $16mm$ (double of PZT diameter), which in turn corresponds to the (actuation) Lamb wave frequency selected, according to the dispersion curves calculated.

Sensor signals from the different transducers of the network are then recorded for each actuation (scan, or inspection). The comparisons between the actual, and potential damaged state, to a reference condition are then performed by subtracting the corresponding sensor signals for those two conditions. Specifically, the sensor signals obtained for those two conditions, for the same sensor, and when the same transducer is actuated, are subtracted. This is performed for all sensors in the network and for all scans,

i.e., for all actuations, meaning for all transducers being actuated, of course, one at a time. With this process, the original excited waves and boundary reflection corresponding sensor signals are removed from the resulting subtracted signal. Signals corresponding to reflections generated by the other transducers in the network and potentially by geometric features and other characteristics of the host material and component being inspected, such as material non uniformity, or structural reinforcements, also disappear in the resulting signal. Furthermore, if the reference state considered had already existing (and known) damages, the reflections generated by those damages are also eliminated from the resulting subtracted signal. Only the signals corresponding to the actual state (to new damages with relation to the reference condition), damage generated wave reflections exist in the resulting signal (and noise).

Damage generated reflection waves can then be identified (damage detection) and their ToF determined. The ToF corresponds to the time of travel of the original, excited wave, from actuator to damage position, plus the time of travel of the damage echo to the sensor which signal is being considered. Knowing the wave propagation velocity (constant for all radial directions in an isotropic material) and the ToF, the total travelled distance can be determined. If the same PZT is used as actuator and sensor, possible damage positions define a circle centered in the considered transducer, with a radius of half the determined total travelled distance. If a pair of PZTs is used, one as actuator and the other as sensor, then possible damage positions define an ellipse with its focus points being the transducer pair considered since the sum of the distances of any point in the ellipse to its two focus points is a constant, in this case, equal to the total travelled distance. Damage position can then be determined as the intersection of the different formed circles and ellipses for all scans performed.

Maximum noise levels, in initial experiments, were verified to be, on average, around 1/1000 of the maximum amplitude of the actuation signal and the low amplitude of damage echoes was around 1/250 of the maximum amplitude of the actuation signal. This low SNR, introduce considerable difficulties in the implementation of the SHM method. Such problems are diminished by the fact that for each inspection/health condition of the component, with the set transducer network, three actuators are used in different positions, at a time, for each scan with the sensed signals from all transducers in the network being recorded for each scan. For each inspection, three scans are then performed, obtaining three sets of one circle and two ellipses to intersect. Although, more computationally demanding, random noise influence is decreased and accuracy of results is enhanced.

To decrease the influence of noise and potential small errors in actuation

(in obtaining the same trigger time and amplitude for all actuations), the origin of time for all sensor signals, for each actuation, is tuned according to the actuator trigger time, for each scan. Sensor signal amplitudes are also normalized with relation to the actual verified maximum signal amplitude in the actuator PZT signal (maximum amplitude of actuation). Furthermore, since the SHM method is developed around the defined frequency of actuation (the same as the interesting frequency of generated, propagating and reflected waves), bandpass filters are applied to sensor signals (second order Butterworth bandpass filters) and FFTs/inverse FFTs to decrease the influence of off tone random noise (and potential other actuations in other frequencies).

Even with the application of all previous referred techniques, false reflections (positives) still exist in the resulting subtracted sensor signals due to noise. The true damage reflection is then contained in the sensor signal in between different false reflections and being masked by them. The duration of each scan is very small, inferior to $1ms$, already accounting for a time interval between consecutive scans to enable the damping of propagating reflected Lamb waves (second and third reflections from the plate boundaries, etc). Furthermore, memory requirements to record data from tests are in the order of what is usually available in a personal computer. To further decrease the influence of random noise, each scan (or each actuation, for each PZT in the network, for both reference and actual states) is repeated fifty times, i.e., for each scan fifty sensor signals are obtained for each sensor. Statistical operations are then applied to the fifty sensor signals (for the same sensor, actuating PZT and condition), such as averaging and determination of average maximums and minimums (within 90% of absolute maximums and minimums), for each and all times. A signal band is then obtained. To identify the corresponding signal of potential damage reflections, sensor signal bands (for the same sensor and actuating PZT), for both the actual and reference conditions are compared/subtracted. When, the sensor signal band corresponding to the actual state leaves (in more than 50% of its width) the sensor signal band corresponding to the reference state, a signal corresponding to a potential damage echo is identified. The process is then continue according to what was explained before (i.e., determination of ToF, etc).

To decrease the influence of the possible existence of false positives, all detected potential reflections are considered. Sets of circles and ellipses are determined for all potential reflections and intersections are performed, enhancing the indication of the location of the actual damage and decreasing (and eliminating) the indication of false (random) damage positions.

In this process, the computational time required for the determination

of the equations of the circles and ellipses and their intersections is considerable. Furthermore, some potential imprecision in the determination of such equations must be accounted for. This results in a possible space imprecision in the determination of the points contained in circles and ellipses, derived from errors in sensor signal time and consequent imprecision in determined wave propagation velocities and in the determination of ToFs for the corresponding signals for different damage reflected waves. If these errors are of enough magnitude, the different circles and ellipses might not even generate any feasible intersection.

Considering these aspects and to decrease their potential negative effects in the code created to implement the SHM method the plate is meshed numerically. A quadrangular, single layer mesh is applied with a spacing of $5mm$. An array of 300 x 300 (for the $1.5m$ x $1.5m$ plate) is created, corresponding each of its positions to one point in the mesh. In a first approach, circle and ellipse equations are determined and a region of influence of 5mm is created around each circle and ellipse. For each circle and ellipse, each point in the mesh is checked upon if it falls in the region of influence of such circle or ellipse. If this condition is verified a unity value is introduced in the array in the corresponding position. For the subsequently considered circles and ellipses, the unity values are added to the values already existing in the array in the corresponding positions superimposed results. The point in the mesh with higher final value (damage index) will indicate the most probable damage position. In the end, all the values in the resultant, final matrix are divided by the highest value, becoming then a percentage proportional to the highest (equal to one in the position corresponding to the highest value) and lowest probability of damage existing in such region. With this method the determination of damage location is performed with a precision of $5mm$, i.e., it will be contained in a circle region with $5mm$ of diameter, around the determined point in the mesh (related with the mesh spacing).

3.1 Damage Detection: Metallic Plates

The transducer network SHM system was experimentally tested in a $1.5m$ x $1.5m$ x $2mm$ aluminum plate, subject to different boundary conditions, ranging from totally supported (to increase Lamb waves propagation damping), to simply supported and riveted in the boundaries. Experiments were conducted initially in a laboratory setting and afterwards in an aircraft maintenance hangar, with no surrounding noise control and limited temperature control. Experiments were performed with the introduction (cumulatively) of surface and through the thickness circular holes and cuts

(with different orientations), with a maximum dimension of $1mm$, to simulate damage (Figure 4). Damages were inflicted in different positions in the entire plate as can be observed in Figure 5.

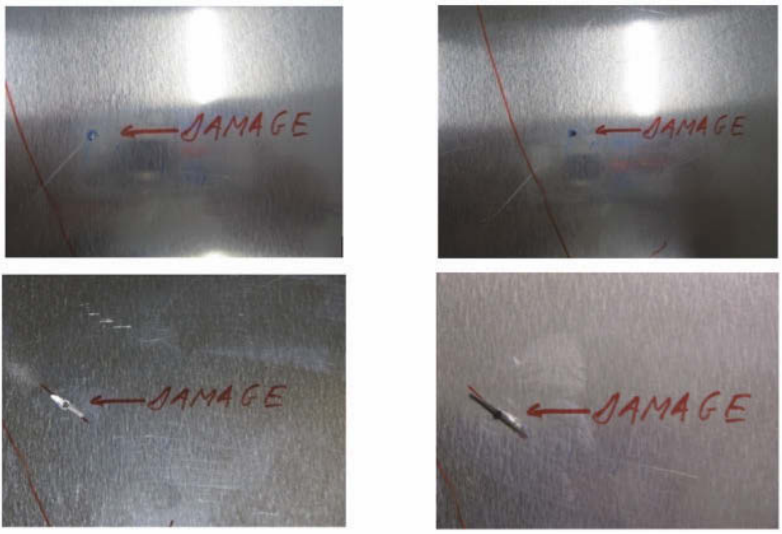

Figure 4. Inflicted damage types

The software for automated inspection was developed in LABVIEW ®, with embedded MATLAB ®codes for signal processing and to implement the damage detection algorithms. The software developed also enables the execution of an initial frequency sweep execution of scans with different frequencies of actuation. Using the position of transducers as an input in the network, in the plate, and plate dimensions, the software calculates the distances in between transducers, and to plate boundaries. With the user input, through the determination of ToF of different direct waves originally excited waves travelling between the actuator and sensors, and boundary reflected waves, during the frequency sweep, it calculates the propagation velocity of S_0 and A_0 waves for the different frequencies. The software determines then the experimental dispersion curves for the usable frequency range within the frequency sweep. The software also accepts as inputs the material/mechanical properties, such as Young modulus, Poisson coefficient and density for an isotropic material, and a thickness for the plate. If requested by the user the software can calculate the theoretical dispersion curves and can compare these with the experimentally obtained curves.

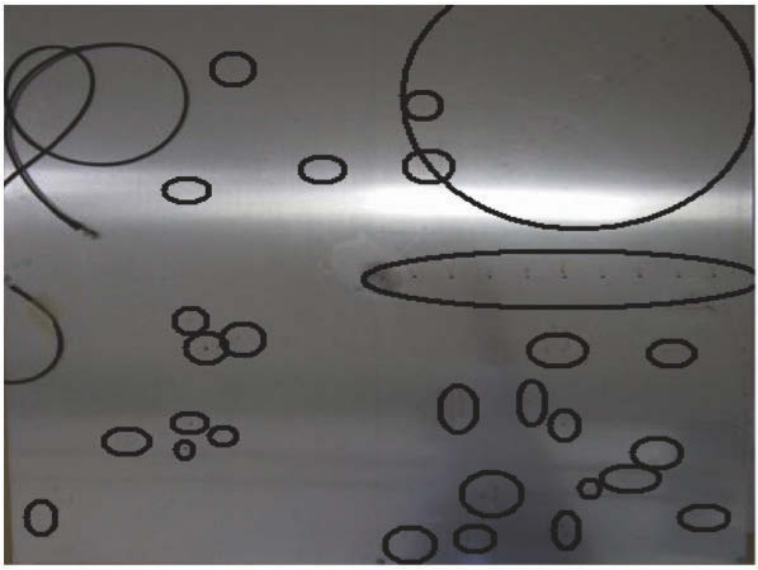

Figure 5. Aluminum plate with all, introduced damages (positions) successfully identified

Based on the experimentally and theoretically determined dispersion curves, it calculates also the wavelengths for the different frequencies. Based on the input for the PZT diameters, it indicates the frequencies at which the actuation and sensing of the S_0 and A_0 modes are enhanced (in which their wavelength is double of the PZT diameter introduced). This indication is backed by an analysis that is enabled to the user by the code, of the evolution of the amplitude of the waves during the frequency sweep. After the calculation of the different wavelengths, the software also presents a tuning curve for the usable frequency range within the frequency sweep. This allows the user to select the optimum (excitation) frequency, and for the determination of wave propagation velocities, to implement subsequently the SHM method.

In the following Figures 6, 7 and 8 the plots presented by the software to the user are depicted. These plots show the damage location algorithm running, i.e., the points corresponding to the circles and ellipses determined for each detected possible damage reflection in corresponding sensor signals (determined through the differences between actual and reference states) for each set of fifty scans when each PZT in the three transducer network is

being actuated. Determined intersection points are also presented. Damage will most likely exist in an area that shows the largest density of intersections (of every color).

To note that in the following figures the plate dimensions are presented non-dimensionalized to 1, and the three transducers in the network are positioned in the following manner: PZT1 positioned in the center of the plate; PZT2 positioned in the middle of the plate boundary presented at the bottom of the plots; and PZT3 positioned in the middle of the plate boundary presented at the left in the plots. In the different plots, it is presented the PZT actuated and the points corresponding to the determined circles (for the actuator PZT) and the different ellipses (determined for the two different pairs of actuator-sensor) are plotted in different colors. Each set of ellipses, determined for each pair actuator-sensor (for all detected potential damage reflections, with each ellipse representing the possible damage positions for each one of those possible different damages), is presented with the same color.

Figure 6 was obtained when a surface cut (with a depth of half of the plate thickness, i.e., of $1mm$), with $1mm$ in length, oriented at $45°$ with relation to the plate boundaries was imposed in the aluminum plate in a position corresponding to the bottom-center position in the figures.

A surface circular hole with $1mm$ of diameter was then drilled in the aluminum plate, in the same position where the previously referred cut was imposed Figure 7.

This circular hole was drilled afterwards through the thickness of the plate. Figure 8 presents the software generated plots depicting the execution of the damage location algorithm (determined points for circles and ellipses, intersection points and most probable location for damage, for all scans), for such introduced damage.

For brevity, only the previous results are presented, however, it must be noted that all applied damages (with $1mm$ of maximum dimension and applied cumulatively to the aluminum plate) were successfully detected and located with the developed automatic SHM system. This was achieved for surface imposed damages, for cuts with different orientations with relation to the transducers in the network and with the considerable (reflection) wave scattering introduced by the round shape/interface of circular holes. Nonetheless, damages introduced behind already existing/imposed defects, in the aluminum plate, far from the implementation region of the transducer network were more difficult to detect and accurately locate. Such difficulties were also verified for cuts, and multiple damages, oriented according to a radial direction, with the centre in one of the transducers in the network, and particularly when aligned with a direction defined by two of the transducers

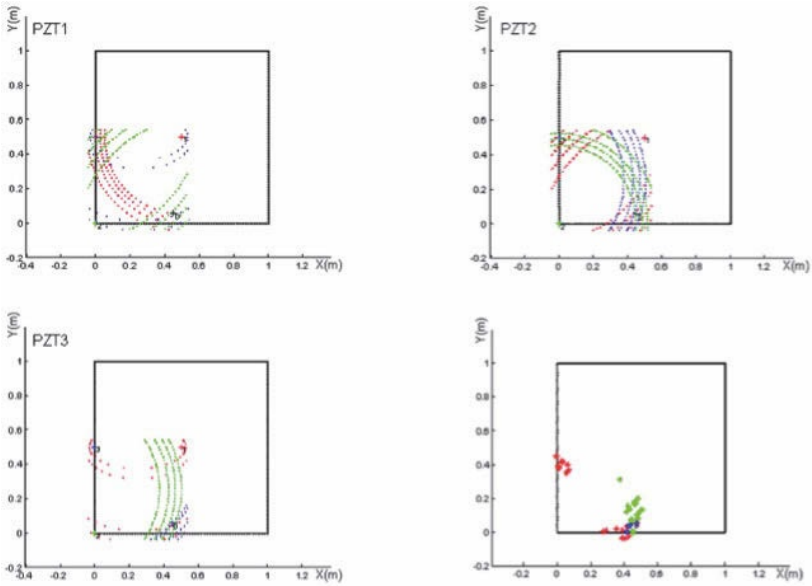

Figure 6. Software generated plots, presented to the user, of the execution of damage location algorithm for a $1mm$ cut imposed in the aluminum plate

in the network (and even more difficult when introduced in regions farther from the area of implementation of the network).

The capability of the transducer network to detect the different introduced damages, and one of its advantage, is related with the fact that by being a network of transducers in considerably different positions in the plate, the actuation origin is changed considerably when the different transducers are actuated. Sensing capabilities of the global network are also enhanced due to the same fact, improving the accuracy in the implementation of the triangulation methods for damage position determination. For instance, for this configuration, it is impossible for cuts, or multiple damages to be aligned with all transducers in the network. The capability of this system to detect damages introduced cumulatively is related with the possibility, enabled by the system, to perform comparisons of the actual state sensor signals with any previous recorded sensor signals, corresponding to different health conditions, including the ones in which previous damage already existed. This enables the capability of detecting new damages, by comparison with the sensor signals obtained for the last inspection (the last state, just

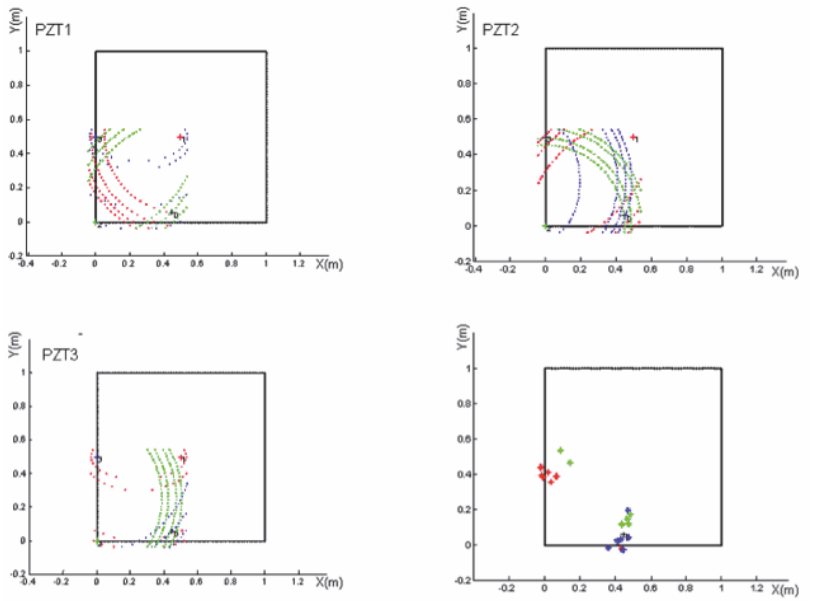

Figure 7. Software generated plots for a $1mm$ surface circular hole

before the actual inspections, or determined condition). This might also enable future damage growth monitoring. The successful detections, and damage location determination, were achieved although the small actuation capability of this system, based in the single actuation of single transducers at a time, and then small excited waves amplitude and consequently much smaller reflection waves amplitude this is, in fact, the main disadvantage presented by a transducer network.

Particularly for riveted boundaries, i.e., for when experiments were performed with the aluminum plate boundaries riveted to a support, some attention was dedicated to inspect such boundaries (conditions). The plate was riveted at its boundaries with two (staggered) rivet lines, spaced $30mm$ apart. The same spacing was used in between rivets in the same line and aerospace grade cherry-pop rivets, $2mm$ in diameter, were used. Inspections were executed to detect and locate loosen rivets, cuts introduced in between rivets and initiating in rivet holes. Any of these introduced types of defects were only successfully detected and (approximately) located when rivets in the interior rivet line (with relation to the plate center) were considered. The inner rivet line scatters the propagating waves with no waves with sig-

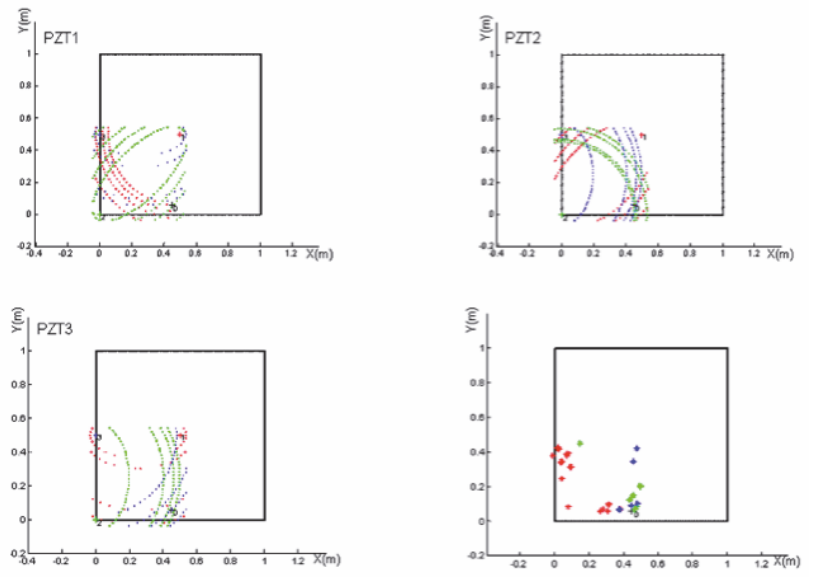

Figure 8. Software generated plots for a 1mm through the plate thickness, drilled circular hole

nificant amplitude propagating beyond those even more true if the already much smaller amplitude of damage reflections are considered. Regarding cuts initiating in rivet holes, these were successfully detected, as long as they are not behind the rivets with relation to the network, i.e., when they were oriented to the interior of the plate, towards the network location. Specifically, cuts aligned with the network were only detected when their length was over $2mm$, due to a minimum required time separation between the detection of their reflection in the corresponding sensor signal and the contiguous rivet hole generated reflection. The minimum required separation time is dependent on the maximum sampling frequency of acquisition of the sensor signals by the oscilloscope (NI digitizer), in this case $60MS/s$, and the wave propagation speed - and also on the minimum number of sampled points for the software reliably determine the existence of such reflection (considering the interference in terms of amplitude between the reflections from the cut and contiguous rivet hole).

At a later stage, an aluminum L stringer was riveted to the plate in the opposed quadrant, with relation to the quadrant of implementation of the network, and perpendicular to a radial direction with center in the center

PZT. The stringer had a height and base width of $30mm$, a thickness of $2mm$ and a length of $500mm$. It was riveted with a single line of rivets, spaced $50mm$. Aerospace grade cherry-pop rivets, with $2mm$ of diameter, were used (as for the riveted plate boundaries). Similar experiments were performed, with similar final results, as the ones regarding the riveted boundaries, described before, i.e., concerning loosened rivets, cuts introduced in between rivets and initiating in rivet holes. The main objective of the introduction of this riveted stringer was to assess the capability of the transducer network based SHM system to detect damage beyond the introduced riveted stringer (and riveted line). All experiments executed proved to be unsuccessful, with no damage imposed beyond the stringer, with relation to the transducer network (application region), being detected. This is explained by the small amplitude of actuated waves and consequently of (damage) reflections, due to the single actuation of single transducers, at a time, in this configuration. The rivet line and stringer completely scatter the excited waves propagation pattern, with no waves with significant amplitude propagating beyond those even more true if the already much smaller amplitude of damage reflections are considered.

3.2 Development of a PCB Board for System Automation

During the experiments executed and presented before, the cables connecting the actuation board and the transducers had to be constantly changed, depending on the actuating PZT since the signal generator used only has one output channel. Furthermore, it was verified that the signals corresponding to reflections, in the actuator PZT sensor signal (i.e., when this transducer was being used as a sensor, just after being actuated), presented amplitudes considerably inferior to the ones verified in the signals of the remaining sensors in the network. This fact created increased difficulties for the damage detection and location algorithm, i.e., for the SHM system, in terms of the detection of such reflections, due to their small SNR, being masked by noise.

Those smaller amplitudes of the signal of the actuator PZT, when used as a sensor after actuation, are related to a mismatch impedance between the actuation and acquisition equipment. The actuation equipment has an impedance to ground that can be configured for 50Ω or 70Ω. This small impedance is required to enable the generation and output of signals with high slew rates, at high frequencies, with small sampling times and high amplitudes. The impedance to ground of the digitizer is $1M\Omega$. A high impedance is desirable to improve the accuracy of data acquisition (based in the measurement of voltage differences, and swings, in between the termi-

nals of such resistance). The ground for the entire system is the same. When a PZT is connected to both equipments (such as the actuator PZT, since the PZTs used as sensors are only connected to the data acquisition equipment) and is being mechanically excited, generating charge (current and voltage) due to piezoelectric effect (PZTs being used as sensors), the current generated will flow to ground through the path with smaller impedance, in this case through the signal generation equipment. This means that for the data acquisition equipment, charge (again current and voltage) is escaping to ground through the actuation equipment. The voltage difference to be measured at the terminals of the resistance in the data acquisition equipment is then smaller.

To solve these two problems, a Printed Circuit Board (PCB) was developed. This board consists of a Micro Control Unit (MCU), an analog signal amplifier circuit (OpAmp) and two Integrated Circuits (ICs) with four switches each. This board is then positioned in between the single channel output of the signal generator and the different actuation channels for the different PZTs in the network. The developed circuit and final PCB, with components mounted and ready to use is presented in Figure 9. To test the developed PCB, a new aluminum plate (with the same dimensions as the previous one) was used. The same transducers and algorithms were applied and similar experiments as the ones presented before were executed. The main difference, besides the use of the PCB, was the introduction of a fourth PZT in the network, positioned in the corner of the aluminum plate (in the quadrant of application of the network). The introduction of this fourth transducer was done to improve the accuracy of the previous network and as a preparation for the application of such PZT network SHM system to composites. It must be referred that after the application of the developed PCB, the amplitude of the signals corresponding to wave reflections, in the actuator PZT sensor signal, were increased by more than 6 times.

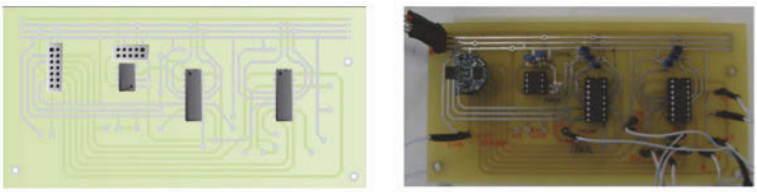

Figure 9. PCB for application in the PZT network SHM system

3.3 Damage Detection: Composite Plates

Composites present different mechanical properties in different directions (anisotropy) and consequently excited Lamb waves present different velocities (wavelengths and dispersion curves), dependent on the direction considered. For the application of the developed SHM system based on a PZT network into composites, damage location algorithms had to be adapted accordingly. In this case, the circles and ellipses determined for damage location degenerate in shapes established according to the different wave propagation velocities in different directions (Figure 10).

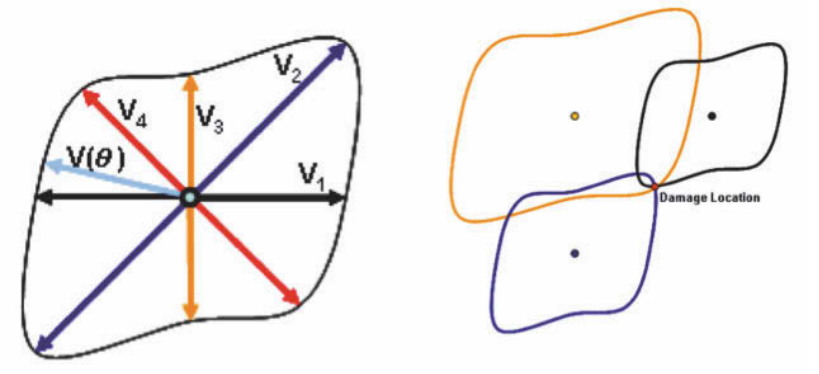

Figure 10. Wave velocity distribution estimate for composite materials

In the initial frequency scans performed by the code, wave propagation velocities (wavelengths and dispersion curves) are now determined for different radial directions in the plate (Figure 11). This is performed with the interaction of the user and analyzing the sensor signals corresponding to the direct excited waves, in between the different transducers in the network, and the plate boundary reflections (using their ToF). The application of a four transducer network becomes of importance to improve the determination of the wave propagation velocities in more radial directions. In terms of the direct waves, the network allows for the determination of such propagation velocities in the directions connecting pairs of transducers. In terms of plate boundary reflections, wave propagation pattern must be tentatively reconstructed, with the determination of the waves propagation velocities in additional directions.

After the determination of dispersion curves (wave propagation velocities and wavelengths for different frequencies) in the different directions, tuning curves and using the method described, are also determined for the different

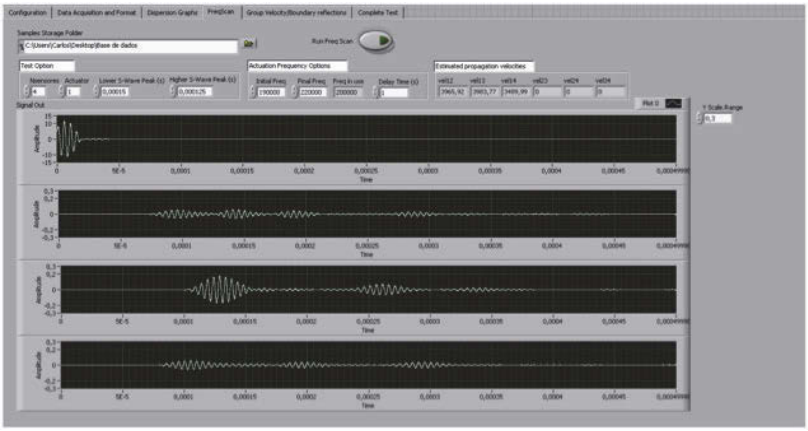

Figure 11. Frequency scan module

directions. These tuning curves will point the frequencies that should be avoided and the ones that tune the SHM system, enhancing the actuation and sensing of the S_0 waves and decreasing the actuation and sensing of A_0 waves, for the different directions. The selection of the (actuation) frequency to base the method upon is performed by the user, with the help of the code. For the diameter of the PZTs being used and for each direction being considered, the frequency that corresponds to a S_0 wavelength double of the PZT diameter being used is determined (to enhance actuation and sensing of S_0 waves). An average frequency should be selected, taking into account also the tuning curves obtained. The results in terms of the selected and analyzed frequencies can also be confirmed by the observation of the waves corresponding signal amplitude, during the frequency scan. As explained before, if the selected frequency corresponds (or is close) to a wavelength that is double of the PZT diameter used, such wave actuation and sensing will be enhanced, and then the waves corresponding signal amplitude (in sensor signals) should be increased. Frequencies corresponding to the highest amplitudes of the S_0 waves signals in sensor signals, during the frequency scans - and preferably lower amplitudes of A_0 waves, are desirable.

It must be noted that the PZT diameter selected a priori may not be the optimum, or even adequate, for this SHM method. To guarantee that, a previous study, with relation to the selection of PZTs and application of the SHM system, should be performed, regarding the composite panels to be inspected. Analytical and numerical methods can be developed to determine

the properties of the material and Lamb wave propagation velocities in the different directions. Assumptions and simulation errors must be diminished at all costs, however, these will introduce potentially significant errors in such determinations, and then in the SHM method. The plates can also be characterized experimentally, with the material mechanical properties (and then Lamb wave propagation velocities) being determined in the different directions through tensile tests, etc. Samples of the material must be used, with potential differences in properties, due to (errors or small changes in) their manufacture, and must be tested in different directions. Lasers can also be used to excite and acquire Lamb waves in the component to apply the SHM system on and potentially dispersion curves - propagation velocities and wavelengths for different (excitation) frequencies - will be obtained in different directions. Tuning curves could be determined and together with the dispersion curves an optimum PZT diameter and (actuation) frequency (averaged for the different directions) could be established.

With the determined propagation velocities of interest, in the different directions, a spline is fitted to approximate the propagation velocities in all directions. The plate is then numerically meshed by the code, in the same way as presented before (with the same mesh, spacing, number of nodes, etc). For each node in the mesh, the radial directions connecting such node and the transducers in the network are determined and consequently wave propagation velocities are obtained in those directions. Knowing also the distances between the considered node to the different transducers, the ToF of a wave travelling between those points is calculated for each node and related with each transducer in the network. With this information, sixteen matrices are set. In each matrix, a node in the mesh corresponds to one of its positions. Each matrix is related to each possible scan to be executed, i.e., with each specific PZT in the network being actuated and with the sensor signal being retrieved from each of the four different transducers, i.e., with each actuator-sensor transducer pair. The different matrices are then populated with the corresponding combination of ToFs previously calculated. For the matrix related with the actuation of a certain PZT and the sensor signal being obtained from a specific transducer in the network, i.e., for a specific pair of actuator-sensor transducers, the matrix position corresponding to a certain node in the set numerical mesh is populated with the sum of the ToFs previously calculated for waves travelling between the actuator and point in the mesh, and between that point and sensor. This corresponds to the total ToF, i.e., the sum of the ToFs of the excited wave, until it reaches the point in the plate considered, and a reflection wave departing such point (as if a damage existed in such position), until it reaches the sensor considered.

With this information, when damage detection and location algorithms are executed, comparing the sensor signals corresponding to the actual and reference states for a determined scan, i.e., for a determined actuator and sensor pair; and after the identification of potential signals corresponding to damage reflected waves and the determination of their ToF, this value (ToF) is compared with the values (ToFs) in each position of the matrix corresponding to such actuator-sensor pair, i.e., to such scan. In this comparison it is verified if the first ToF referred falls in between certain positions of the matrix in consideration, with these boundary positions being considered as potential damage location candidates. The remaining process explained before, for the developed SHM system is implemented (formation of damage indexes, probability, intersections, scan repetition, filtering, etc).

After adapting the developed SHM system for its application to composite material plates, accordingly to what was explained before, experiments were performed in a $0.48m$ x $0.48m$ CFRP material plate. This plate has a thickness of $1.6mm$, resulting from ten layers of carbon fiber weave in the following laminate lay-up: [(0/90)/±45/(0/90)/±45/(0/90)]S. By possessing an uneven ratio between (0/90°) and ±45 ° layers, the plate presents a higher stiffness (or Young modulus) along the 0/90° directions, being expected to obtain higher wave propagation velocities along the 0/90° directions, with relation to the ±45° (and all other) directions.

A four transducer network SHM system was implemented into the composite material panel, using similar PZTs as before, in the following configuration, presented in Figure 12.

From the initial frequency scans performed for this case, by the SHM system, a frequency of actuation (and to base the SHM method on) of $210kHz$ was established. For this frequency, the S_0 Lamb wave (mode) propagation velocities, determined with the help of the program, in different directions connecting the different transducers in the network (and principal directions in the plate), i.e. for the direct excited waves, are presented in Figure 13.

Observing the calculated S_0 wave propagation velocity by the code, it can be verified that the propagation velocities obtained for each PZT pair, when one is used as an actuator and the other as a sensor and then their function is alternated, are similar. Propagation velocities obtained for the 0/90° directions are similar and higher, as expected, for the reasons explained before, than the velocities obtained for ±45°. Regarding the velocities obtained for the 135° direction, these are similar for both pairs of PZTs (1 and 4, 2 and 3). However, significant different values of such propagation velocities were obtained for the 45° direction, depending on the pair of transducers being used (pair PZT1 and 2 with relation to PZTs 3 and

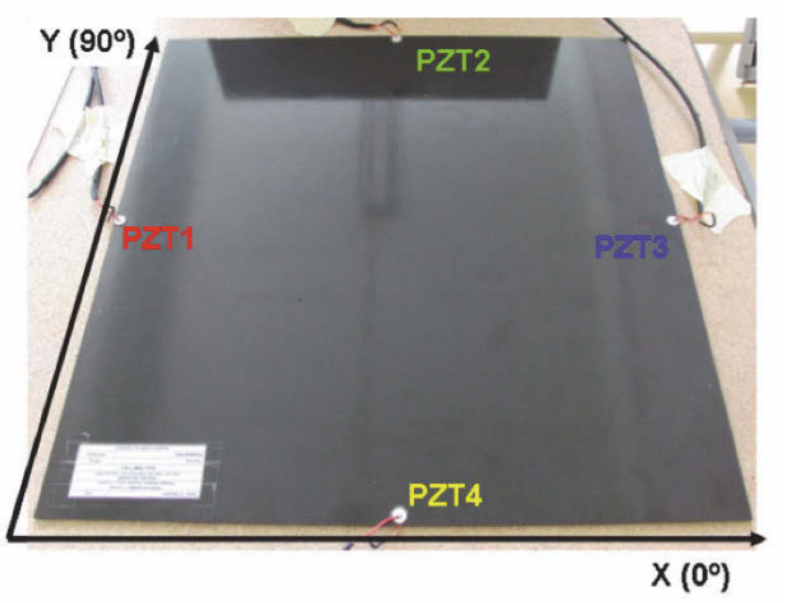

Figure 12. Composite panel, transducer network and experimental setup

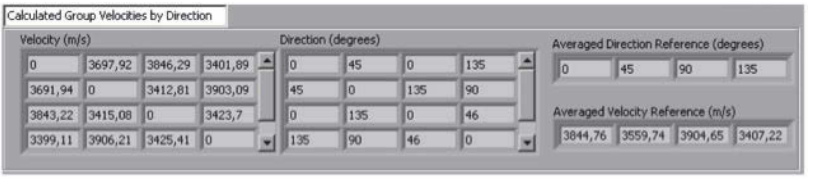

Figure 13. Propagation velocities obtained from the code for different directions

4). Furthermore, since a $\pm 45°$ weave was used, the velocities along 45° and 135° directions should be similar, this is verified when considering the pairs of PZTs 3 and 4, with relation to PZTs pairs 1 and 4, and 2 and 3, but not when comparing all previous pairs with the pair 1 and 2. Unexpectedly, the propagation velocity results from the pair of PZTs 1 and 2 are about 7% higher than those obtained with the remaining pairs referred before. This may result from errors in the manufacture of the composite material plate - manually manufactured. The fact that the weaves were manually laid and no particular control on resin flow was possible may explain the differences in properties at 45°, depending on the area of the plate considered. The velocities for each direction were averaged, and then the velocities of propagation for 45° were also averaged. The considerable differences verified at such direction (due to manufacture imprecision), depending on the location in the plate, and the fact that an average velocity must be used, will introduce errors in the damage detection and location algorithms (although the use of an average velocity tends to decrease existing errors).

Fitting a cubic spline to the average propagation velocity values calculated for the different directions, a velocity distribution can then be estimated for all directions in the entire plate. This is shown in Figure 14.

With this velocity distribution, damage detection and location experiments were then performed. The steps described previously, for the execution of the SHM method, were followed, with the reference or undamaged condition of the plate being characterized (through the execution of the different initial scans). Afterwards, a through the thickness hole of $1.5mm$ in diameter was drilled in the plate at a location ($0.17m$, $0.17m$), considering as a reference the coordinate system indicated in Figure 12, i.e., with its origin in the bottom left corner of the plate. Scans were then executed and the actual damaged state was characterized with the damage detection and location algorithm (described before) being executed afterwards. The execution of the damage detection and location algorithm can be seen in Figure 15, as presented to the user by the developed software. Notice the degenerated circles and ellipses as a result of the dependence of propagation velocity on direction.

The final plot/results (software output) are presented in Figure 16, for this case.

The observation of the final plot by itself is not revealing in an easier and direct manner of the existence and location of damage. However, the observation of the plot together with (and particularly of) the resulting table reveals that the system was capable of detecting and determining three positions in the plate with a higher probability of damage existence. Even though such probability is not considerably high and is just slightly

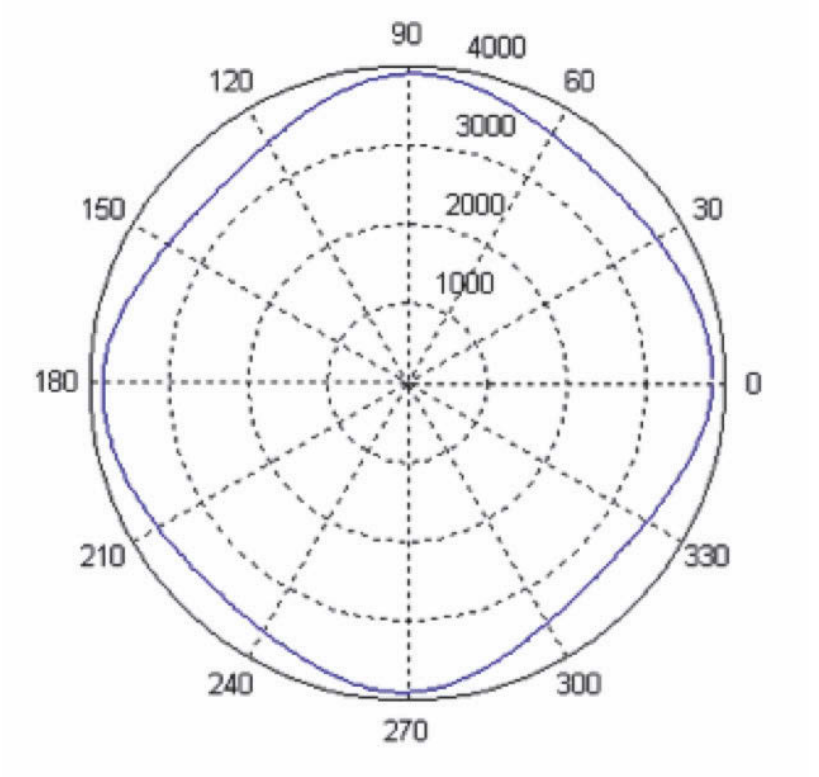

Figure 14. S_0 wave propagation velocity radial distribution

higher than the one determined for the next possible seven candidate points for damage existence; and the system also determined two false positives; the imposed damage was also detected and located.

With the results obtained, noise threshold levels were tuned within the software and newer results are plotted in Figure 17. As it can be observed, also false positives were determined, however the introduced damage was detected and successfully located, obtaining a stronger indication.

3.4 Initial Acoustic Emission Experiments

The idea to execute initial experiments for the detection of Acoustic Emissions (AE), with the implemented SHM system, stemmed from the fact that this system must already be deployed, i.e., a set of PZT transducers is

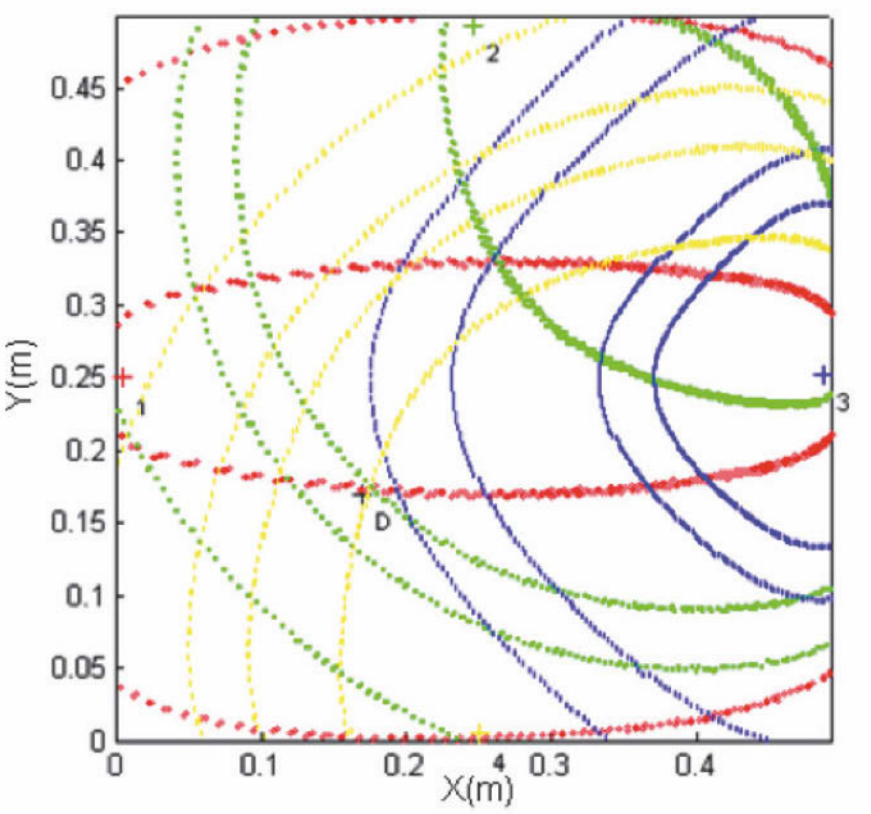

Figure 15. Damage detection and location algorithm

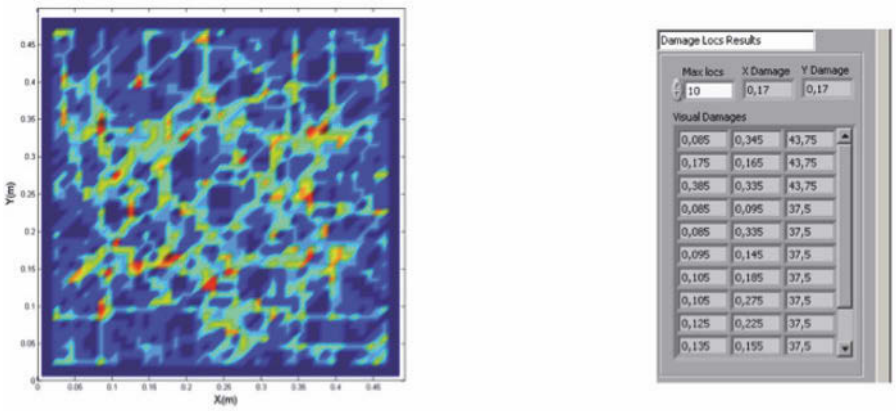

Figure 16. Software output

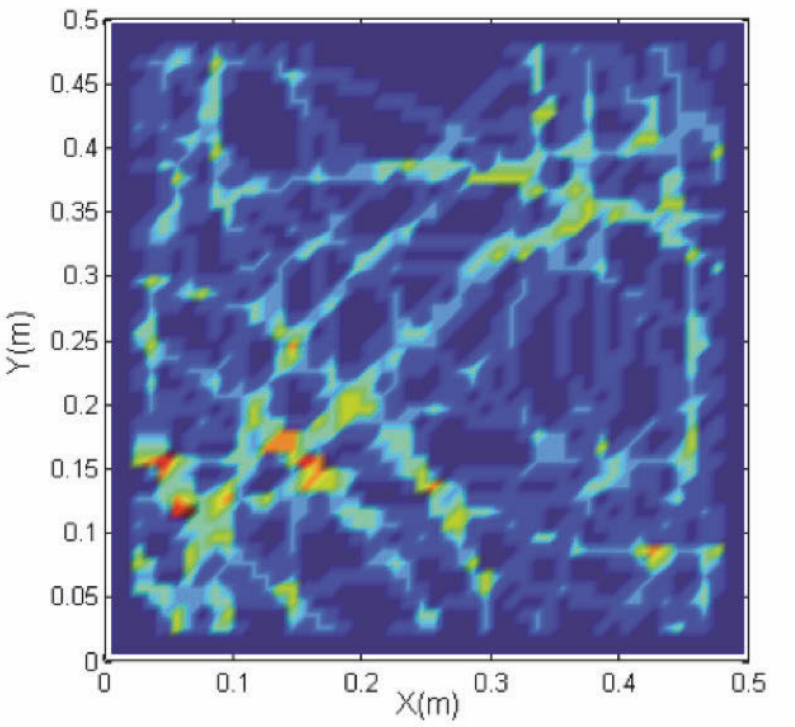

Figure 17. Results obtained after noise threshold levels were tuned

already positioned in the component to inspect and available with the SHM system being executed only at certain times. There is then the possibility to use such system and transducers continuously, in between the execution times.

With the developed SHM system based on a four transducer network, initial AE experiments were performed in an aluminum plate identical to the ones used before, but with the system being used in its passive mode, i.e., no actuation was applied, with the actuation system being disconnected from the network transducers (just connected to the data acquisition system). The software developed was adapted to acquire transducers signals continuously, and just starting to record data from the four sensors, when triggered by detecting the first corresponding signal to a wave in one of the sensor signals. After such detection occurs, the code verifies if it can detect signals corresponding to such wave in the other three sensor signals. If it

doesn't, it neglects such data and goes back to the initial state. If signals corresponding to a wave are also detected in the other three sensor signals, data is conserved and a developed damage detection and location algorithm is started.

After the software detects the initial triggering wave corresponding signal, it saves data during $500\mu s$. This value was determined with the following considerations:

- knowing that the system is searching for a wave that was generated by an impact in the plate (possibly also simulating the growth of an existing damage) and not a reflection;
- considering the diagonal of the plate used ($1.5m$ x $1.5m$) as the highest distance between a possible AE origin and any transducer of the network (in this case the corner PZT);
- the SHM system was developed to detect (and then it will only try to detect, or better was optimized to detect) λ_0 waves with a frequency around $340kHz$, i.e., the frequency that, through the previously determined analytically and experimentally obtained dispersion curves for the aluminum plate (as explained before), corresponds to a wavelength double of the PZTs diameter being used, optimizing its sensing (and also according to the tuning curves calculated and frequency scans). The λ_0 waves in the aluminum plate with the referred frequency of $340kHz$ have a propagation velocity of $5390m/s$, as determined before. It must be remembered that the developed system applies passband filters to the acquired data, around such frequency. It can be concluded that the system will search for AE only as Lamb waves, in its first symmetric mode (S_0), with a frequency around $340kHz$;
- the determined value exceeds the calculated value according to the distance and velocity previously referred, for safety.

For the detection of such waves (and to trigger the system), a noise threshold was defined. In the location method to be presented next, multiple detected potential waves are considered for each sensor signal, as before, including false positives due to noise.

After detecting such waves, and since (there is no dedicated actuation) the original time of actuation, i.e., the time at which the AE was generated in its origin point is unknown, it is not possible to use that as a time reference or origin. The initial time at which the system was triggered (by the first wave detected) is then considered the origin of times. Also, due to the fact that the time at which the AE was generated in its point of origin is unknown, the location method must be based in time differences between the different detected waves in the different sensor signals, i.e., relative, or differences in their ToF. With the propagation velocity considered,

these ToF differences can be translated in differences of distance travelled by the AE between the different sensors in the network. Based on this information, hyperbolas can be determined for each pair of sensors and for all (combinations of the different) detected potential waves combinations are formed with the data from one wave detected by one of the sensors of the pair and the data from other wave detected by the other sensor in the pair. Such hyperbolas represent the locations in the plate that the distances to the pair of transducers considered are related by the determined differences (traveled by AE to the different sensors).

The location algorithm, previously based on circles and ellipses, is now adapted to the referred hyperbolas. The remaining algorithm, with the meshing of the plate and search algorithm is used to obtain the intersections of such hyperbolas and then determine each candidate position for damage existence and the corresponding probability.

The generation of AE was simulated by dropping a steel sphere, of $10mm$ in radius from a height of $15mm$ (from its center) with relation to the plates surface, in different positions in the plate. Due to the small amplitude of generated AE, these were detected and their origin successfully located in 50% of the experiments performed.

4 Phased Arrays

Earlier, experiments were performed with the implementation of a PZT network for SHM applied to aluminum and composite material panels. During that study the small amplitude of generated and consequently (boundaries and damages) reflected Lamb waves was verified. Particularly, damage generated wave reflections were of extremely small amplitude and prone to noise interference making them more difficult to detect (in corresponding sensor signals). Aggravating this fact, damage reflection wave amplitudes decrease considerably when smaller damages are considered, introducing paramount difficulties when trying to decrease the detectable minimum damage dimensions. Furthermore, it was verified that with the small amplitude of the excited waves and subsequent reflections (generated by a single transducer), damage beyond structural reinforcements and riveted lines (with relation to the system location) were not detected. Such features scatter the excited waves propagation pattern (and energy), creating reflections, and with no waves with significant amplitude propagating beyond those, for the small wave amplitudes (energy) involved.

This is related with the single actuation of a single transducer (at a time) that occurs in a transducer network. A possible way to increase the amplitude of emitted waves would be the use of actuation signal amplifi-

cation with the use of amplifiers. This solution introduces, however, two main difficulties: inclusion and amplification of noise with relatively small improvements in SNR and the fact that the actuation signal applied in the referred experiments (in the range of ±18V, permitted by the maximum output swing of the signal generator) was already close to the maximum voltage and charge permitted by the PZT transducers. Previous experiments resulted in the depolarization and damage of the small transducers when the actuation signal was amplified to a range of ±21V.

The solution to increase amplitude levels of actuation and reflection waves (specifically of damage, when smaller sizes have to be considered in order to reduce detectable damage dimensions) was then to use multiple actuation. The objective is then to promote constructive interference in predetermined positions of the plate between the waves excited by several single actuators (beam forming, or generation of a wavefront). Since actuators will have to be in different positions on the panels a phased actuation is necessary. The phased actuation implies that small time delays will be introduced in between the actuation of neighbouring transducers. The time delays to introduce are related with the relative positions at which the transducers are applied on the plate (configuration of the array), the distance between them (considering a linear array, its pitch), the propagation velocity of waves to excite and the propagation direction of the generated wavefront. By varying the time delays the wavefront propagation direction can be modified (steered). Inspection can then be focused into predetermined regions of the component. By modifying time delays in between different scans the component can be entirely inspected.

In the PZT network experiments, a National Instruments (NI) PXI-5421, $100MS/s$ Arbitrary Waveform Generator with 16 Bit resolution, $8MB$ of internal memory and a single output actuation channel was used for signal generation and actuation. Due to the high propagation velocities of Lamb waves to excite, in order to achieve successful constructive interference, time delays to be introduced will be extremely small. This means that even when phased actuation is considered, at certain times multiple transducers will be actuating simultaneously. The implication of this fact is that a single actuation channel simply demultiplexed cannot be applied. Delay circuits would then have to be considered, with the introduction of noise and imprecision in the establishment of time delays. The conclusion is that multiple actuation channels are required. As stated before, besides presenting extremely high cost of acquisition, existing systems with multiple actuation channels commercially available, or under research, suffer either from:

– Not offering enough precision in time definition for the correct es-

tablishment of smaller time delays required for the generation of fast propagating S_0 wavefronts. Some of the commercial available systems are capable only to establish the correct actuation signal to generate S_0 waves in a single channel at a time, while phased array systems under research generate slower propagating A_0 wavefronts, relaxing the requirement of high definition in time, since to generate slower wavefronts, the time delays to introduce are higher;
- or not even being capable of the generation of the correct actuation signal for each individual actuator, in terms of time or (higher) frequency definition or at least not offering the capability of the user to define such actuation signal (black/closed box systems), either in terms of waveform or frequency selection, restricting its application to certain conditions, materials and components.

The obvious conclusion is that a lower cost, dedicated multiple channel actuation system had to be developed. The system must be capable of a high time definition to precisely establish the required small time delays in between consecutive channels/transducers to be actuated for the correct generation of the fast propagating S_0 wavefronts and the correct actuation signal waveform and (high) frequency for the generation of the single, fast S_0 waves by each transducer.

For the reasons stated previously, PZT transducers were selected to be applied in the phased array SHM system. This selection is based on the fact that a single PZT transducer can be used as an actuator and as a sensor. Furthermore, PZT transducers can be used in techniques involving high frequency generation and sensing. As the basis for a future development of arrays with different configurations (cross, star, circular shapes, etc) it was decided to implement a linear array to excite fast propagating S_0 wavefronts (the selection of this wave mode was based in the reasons stated before). A linear array presents advantages in terms of a simpler development. At the same time, different array configurations can be seen as a combination of multiple linear arrays, while solving the disadvantages in terms of inspections introduced by a single linear array (also referred before).

To simplify the implementation and testing of this phased array SHM system in development. The initial application was to aluminum plates (isotropic materials, with homogeneous properties and then constant wave propagation velocities in all directions). However, in its development it was also considered its future application to panels made of composite materials (orthotropic), presenting different mechanical properties in different directions and then with wave propagation velocities depending on the direction considered. This fact became important even for the experiments executed in aluminum panels, since, due to their manufacturing processes mechan-

ical properties are not exactly the same in all directions. Small relative differences in properties exist, for instance due to the lamination direction in aluminum plates. These small relative differences are translated to considerable absolute values when the high values of Young modulus and wave propagation velocities are considered. In the previous experiments with the PZT network SHM system, differences around $200m/s$ (however less than 0.5%) were verified in the propagation velocity of the S_0 wave in aluminum plates in different directions.

The development of the phased array SHM system accounted for its future implementation in real structural panel components in the sense that it was considered, in its development, its experimentation in representative plates with more stringent boundary conditions. For instance, experiments with the plate totally supported (increasing wave propagation damping), with simply supported and riveted boundaries were considered.

Furthermore, experiments were considered to be performed in environmental conditions close to reality. Some experiments were considered to be executed in an aircraft maintenance hangar, without any surrounding sound/noise control and with limited temperature control.

4.1 Dispersion Curves

As referred before, the experiments involving phased arrays were performed in aluminum plates identical to the ones used before, for the implemented transducer networks same material, thickness and remaining dimensions. Due to this fact the dispersion curves, and all data, and considerations presented earlier are applied here.

Regarding the implementation of phased arrays, so that undesirable side lobes are not generated, the phased array pitch should be less than or equal to half of the wavelength to be excited (Giurgiutiu, 2008):

$$pitch \leq \frac{\lambda}{2} \tag{22}$$

Since the array pitch is equal to the dimension of one of its PZT transducers plus the spacing in between consecutive elements in the array, the tuning of such system (selection of excitation frequency and wavelength) should now be performed with relation to the array pitch and no longer with relation to the PZT element dimensions. However, it is still true that the amplitude of generated Lamb waves is increased when the dimension of the PZTs used approaches half wavelength of excited waves. The logical conclusion is that the array pitch should be equal to half of the wavelength (to avoid considerable side lobes) of waves to be activated and the PZT transducer dimension should be as close as possible to the phased array pitch,

reducing spacing in between consecutive elements to a minimum. Nonetheless, neighbouring elements should not be in contact (and not even their bonding material). If contact existed, the actuation of one element would be passed to the adjacent element, creating actuation noise and interference on the later PZT. To enforce this condition while trying to minimize the spacing in between consecutive elements of the array, and due to practical aspects, a spacing of $3mm$ was considered to account for $1mm$ around each transducer to be potentially occupied by its bonding material and $1mm$ of effective spacing. This means that it was considered that the PZT elements have a diameter equal to the phased array pitch (equal to half of the wavelength to be excited) minus $3mm$.

4.2 Tuned Lamb Waves: Mode, Frequency and Transducer Selection

The tuning of the phased array system was performed in the same manner as presented earlier. However, the pitch of the phased array must now be considered, instead of the PZT transducers diameter. Tuning the phased array system for the S_0 wave can be achieved by selecting an activation frequency and correspondent array pitch (equal to half of S_0 wavelength to be excited, corresponding to the frequency selected, to enhance S_0 actuation and sensing and not to generate side lobes), and PZT transducers diameter, such that the PZT diameter is a multiple of A_0 wavelength to be excited (to decrease actuated A_0 amplitude and decrease its sensing), again corresponding to the frequency selected (or at least as close as possible to a multiple). To refer that the higher that multiple is, the more the activated A_0 amplitude is decreased.

A tuning curve is now obtained in the following manner: based on the wavelength vs. frequency curves, for all frequencies the S_0 wavelength was halved, with these values being subtracted by $3mm$ (the spacing in between consecutive elements in the array) to obtain the optimum PZT dimensions (to excite and sense those S_0 wavelengths at their corresponding frequencies) as before, the resulting values were then divided by the A_0 wavelengths excited at the same frequencies. Afterwards, the same process as described earlier was applied: the absolute values of the difference between such results and the nearest integers were analyzed and for an easier representation and assessment of those results, those differences were doubled and the results were subtracted to unity (values to be presented close to one represent optimum conditions and values close to zero the worse cases). The resulting tuning curve for the phased array is presented in Figure 18.

According to this curve, activation frequencies around $150kHz$ (and cor-

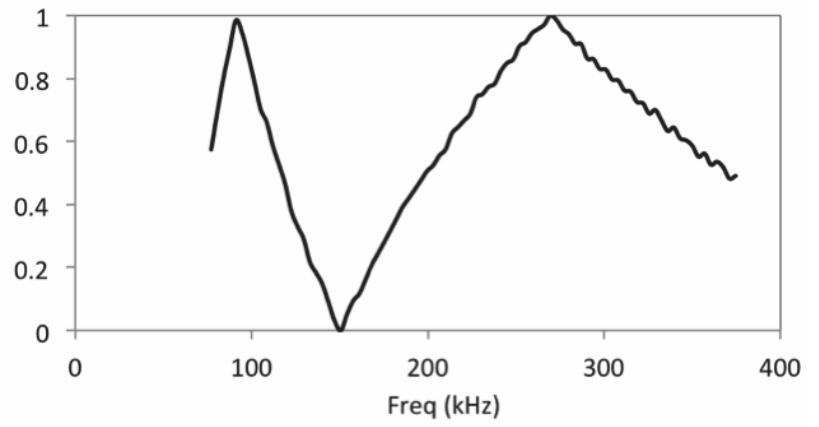

Figure 18. Lamb wave tuning for the phased array system

respondent wavelengths, array pitch and PZT transducers diameters) should be avoided, while frequencies around $100kHz$ and $275kHz$ give the best results. It must be remembered however, that the application of smaller wavelengths is desirable for the detection of smaller damage dimensions, what is achieved at higher frequencies. The frequency of excitation should then be selected to be $275kHz$. However, due to their availability the same PZT transducers applied before in all experiments were used with a diameter of $8mm$. Considering the spacing in between neighbouring elements in the array of $3mm$, this corresponds to an array pitch of $11mm$ (which should be equal to half of the wavelength of the S_0 wave to excite). The corresponding actuation frequency is then $245kHz$ with the S_0 waves of that frequency presenting a propagation velocity of $5450m/s$, in the considered aluminum plate.

To refer that due to the same reasoning as presented earlier, the same actuation signal waveform is used for the activation of each PZT element in the phased array. Considering the actuation frequency of $245kHz$ (inner sine frequency) the actuation signal will have a total duration in time of 20.41μs. According to what was referred to earlier and considering that the S_0 waves of that frequency present a propagation velocity of $5450m/s$, in the considered aluminum plate, a distance of $56mm$ around the PZT transducers (phased array) will not be inspected.

4.3 Number of Elements in the Array

To be able to inspect an entire component, the scans performed by a phased array must be repeated, with the wave front being steered into different directions in the component in each scan. Consequently, different time delays must be applied between the actuation of consecutive array elements in the different scans. To define the directions (and related time delays) that must be considered to enable the inspection of the entire component the aperture of the generated wavefronts must be taken into account. The aperture angle is centred around the propagation direction of the wave front generated by the phased array. It defines the region where such propagating wave front will be effectively formed and then the useful inspection region for each scan direction considered.

Such aperture ($\Delta\alpha$) is dependent on the total length of the phased array (l), the phased array pitch and number of elements in the array (n) and on the excited Lamb wave wavelength (λ) (Giurgiutiu, 2008):

$$\Delta\alpha \simeq 0.886\frac{\lambda}{l} \simeq \frac{\lambda}{n \cdot pitch}(rad) \tag{23}$$

This relation is valid for all angles of the propagation direction of the array generated wavefront (in an isotropic plate), particularly for angles approaching the perpendicular to the linear array. It is predicted that due to the influence of the array elements into the excitation/propagation of the wavefronts these will present lower amplitudes (decreasing inspection capability) and will be more spread in space when their propagation direction approaches the direction of the array (increasing the aperture in those directions). Then the aperture calculated according to Equation 23, can be regarded as the minimum aperture. If such value is considered as the angle interval to be established in between consecutive inspection directions, it will be guaranteed that the entire component can be inspected. Simultaneously, the overlap of inspection regions will be promoted and inspection capabilities will be enhanced.

Theoretically, constructive interference in between generated waves from different transducers in the array is augmented (the amplitude of generated wavefronts is increased), when the number of generated waves and then the number of transducers is increased in the array. However, the wavefronts to be generated will be more spread in space in those conditions. As can be observed from the above equation, such results in a lower aperture of the array. As a compromise, it was decided to implement an array with seven elements.

4.4 Phased Array Actuation System

Regarding the phased array actuation system, a configuration based on a master circuit controlling the phased activation of different slave circuits was implemented. Each slave circuit, when activated by the master, generates the actuation signal to one PZT transducer in the array. The master circuit consists of a simple Micro Controller Unit (MCU). The MCU was selected considering its processor frequency, the output frequency it is capable of and number of output pins. The number of output pins limits the maximum number of slave channels that one MCU is able to control however, two MCUs can be connected to communicate with each other, in order to expand the number of channels to control. The processing and maximum MCU output frequencies determine the minimum time delays that it is capable to apply for phased activation of the slave channels. A Texas Instruments (TI) MSP430F2012 MCU with $16MHz$ of processing frequency, $4MHz$ of output frequency and two output ports, with eight and two pins respectively, was selected the same MCU used in the developed PCB before, for the PZT network SHM system. For the selection of the minimum time delay that the MCU would be able to apply, in this case $250ns$ (corresponding to an output frequency of $4MHz$), a simple exercise was followed. The time delay to be applied in between consecutive actuations (Δt) corresponding to the inverse of output frequency (f_{out}) is equal to the difference in distance travelled by the consecutive generated waves (Δd) divided by the activated waves propagation velocity (V):

$$\Delta t = \frac{1}{f_{out}} = \frac{\Delta d}{V} \tag{24}$$

Through simple geometrical relations depicted in Figure 19, the difference in travelled distances can be related to the phased array pitch and the direction of propagation of the activated wavefront (α) by:

$$cos(\alpha) = \frac{\Delta d}{pitch} \tag{25}$$

Combining the previous two equations:

$$\Delta t = \frac{pitch \cdot cos(\alpha)}{V} \tag{26}$$

Knowing that for a wave:

$$V = \lambda \cdot f_{wave} \tag{27}$$

Assuming that an optimized phased array is implemented such that its pitch is half of the wavelength of Lamb waves being generated:

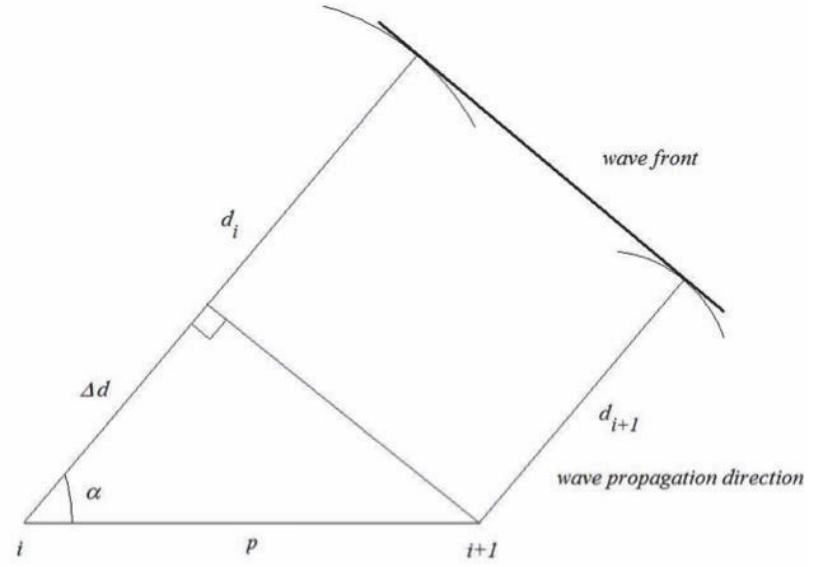

Figure 19. Phased array beamforming

$$\lambda = 2 \cdot pitch \tag{28}$$

Replacing this equality in Equation 27 and the result in Equation 26 , the following relations can be obtained:

$$\Delta t = \frac{cos(\alpha)}{2f_{wave}} \rightarrow f_{out} = \frac{2f_{wave}}{cos(\alpha)} \tag{29}$$

To generate a wave front propagating in a direction perpendicular to the linear array, the master MCU must output simultaneously the activation signals to all slave circuits without any delays applied in between actuations. This means that the MCU must output all pins simultaneously. This is not problematic. The smallest non zero time delays to be applied correspond to scanning directions (to wavefront propagation directions) closest to that normal direction. If it is desirable to inspect the entire component, for the different inspected regions in different scans to be contiguous, the different inspection directions must be spaced by no more than the array aperture. To achieve this the scanning directions closest to the normal of the linear array to be selected will be separated from that normal by the aperture angle. It

is then necessary to calculate a minimum aperture that will correspond to the minimum time delays that the master will be able to apply. Equation 23 can be simplified by assuming an optimized phased array, i.e., Equation 28, resulting in:

$$\Delta\alpha = \frac{2x0.886}{n}(rad) \tag{30}$$

Considering the application of a phased array with a maximum number of seven elements, the array aperture is calculated to be 0.2476 rad, or 14.19°. Considering a little superposition of adjacent inspection regions (for safety), the closest angle to 90° will then be 77°. With Equation 23, the maximum wave frequency that can be applied in the inspection method for the output frequency of the master MCU of 4MHz will be $450kHz$. Such value is higher than the upper limit of $400kHz$ established for the actuation frequency to apply in this system.

It must be noted that the processing frequency of the MCU is also important for the correct implementation of the method since the error in time between the desired time for output and the time at which such output occurs in reality is in the worse situation 20% of its clock period (then $12.5ns$), usually below 10% of the clock period ($6.25ns$).

According to the aperture determined for the array of 14.19°, and as referred for safety reasons, the maximum angle interval in between consecutive directions of inspection was established to be 13°. The inspection direction angles, or the angles at which is intended that the wavefronts will propagate were selected to be 6°, 19°, 32°, 45°, 58°, 70°, 80°, 90° and the symmetric directions with relation to the normal of the array. Angles are measured anti-clockwise with relation to the direction of the linear array, from the right. With the selection of these directions some overlap in between the regions to inspect is promoted. Particularly, the 6° direction was selected to enable the inspection of the region laterally adjacent to the phased array while avoiding the destructive interference of the PZT elements in the array to the propagation of the wavefront in the array direction.

With the selected inspection angles, knowing the propagation velocity of the S_0 waves (and wavefronts) to generate and the linear phased array pitch, the corresponding time delays to be introduced in each scan (for each propagation direction angle) were determined. These delays were then implemented in the developed code to use in the master MCU.

For the design of the slave circuits for the actuation of each PZT in the array, it was also considered a MCU to generate the digital signal corresponding to the actuation waveform (the bit trail). One of the main advantages of the use of such MCU is that as in the case of setting the

time delays for the different scans through the use of the master MCU, it can be programmed so that the actuation signal waveform can be modified, particularly regarding its frequency. This will enable the application of the inspection technique to different materials in the future. The MCUs used in the slave channels were similar to the one used for the master circuit. The number of pins was more than sufficient from the available 10 pins, five pins are needed at the most, one for input from the master, two to output the inner sine function and the modulating window digital signals and between one to three pins to control output switches (depending on the configuration selected by the user). With the designed and implemented technique to generate the actuation signal, the MCU is capable to generate signals with frequencies up to $2MHz$ (half of its maximum achievable output frequency of $4MHz$). The small errors in time introduced in the signal output are related to the MCU processor frequency as it was the case for the master MCU. Some of the tests being performed to the components of the phased actuation system, using a bread board are depicted in Figure 20.

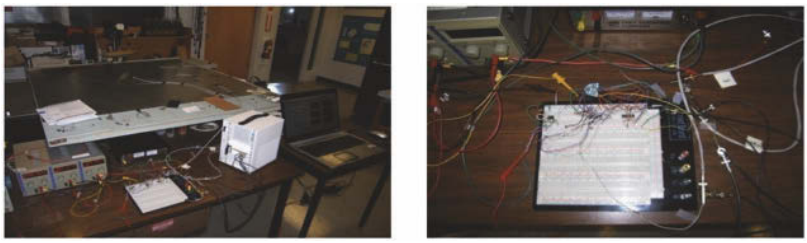

Figure 20. Components of the phased actuation circuit being tested

The slave circuit experimental (non miniaturized prototype) board (and system diagram), with DIP (through hole) larger electronic components is depicted in Figure 21.

4.5 Damage Detection Algorithms

Regarding the damage detection algorithms, two different approaches were followed concurrently. The first was based on the application of the phased array sensing principle referred in the literature review, which is applied by the majority of works in this field. In this approach, since the inspection direction is known, the phased array sensor signals are shifted in time for the corresponding relative time delays. Afterwards, the signals are added with the resulting signal being searched for a potential damage reflection. With this procedure, incoming reflection waves in the inspection

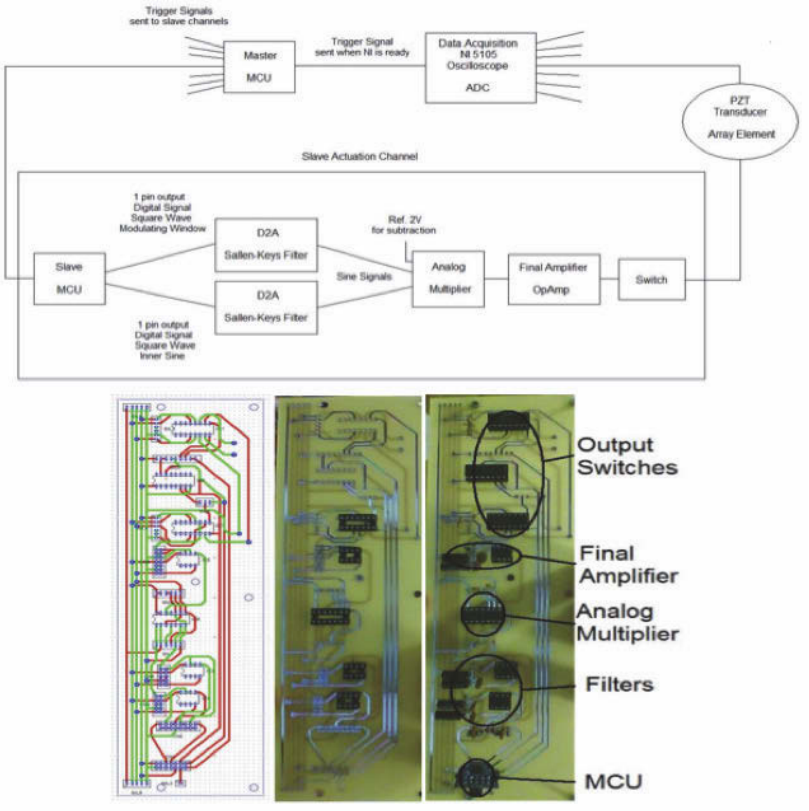

Figure 21. Slave circuit

direction will be enhanced, increasing SNR. After encountering a potential damage reflection damage detection, its Time of Flight is retrieved from the sensor signals (time between the wavefront generation and detection of such reflection). Knowing the wave propagation velocity (equal for generated wave/wavefront and reflections), the total distance travelled by the generated and reflected waves is calculated. The distance between the phased array and damage is then determined, as half of the total distance travelled by the generated and reflection waves. Knowing the inspection direction, damage location is then determined. The disadvantage of this approach is that it is based on the approximation that the incoming damage reflection to the phased array is a (linear) wavefront and not a curved wave, as it is in

reality. This approximation gives acceptable results for the determination of damage location when the damage is sufficiently far from the array and the section of its reflected wave arriving to the phased array is approximately linear. However, when damages are close to the array, damage location is not accurate enough.

This approach can be used with either a single or a phased array actuation and can be applied in a supervised or unsupervised method. In the supervised approach, the (potential damage) reflections are searched for directly in the sensor signals obtained from scans for the current health condition of the component being inspected. There is no need in this mode of previously saved signals for a reference state (undamaged or with known damages, to monitor new damages and damage growth) and then no subtractions or comparisons are done. Since no subtractions are performed, the current signals to be analyzed will present all reflections from boundaries and other intrinsic geometric or material discontinuities in the component. To distinguish a potential damage reflection from these reflections a supervised approach is required.

In the unsupervised approach (as used for the networks experiments) with the execution of subtractions between current and reference signals potential damage reflections are enhanced (with relation to the disappearing boundary reflections) and easier to detect in the sensor signals. Besides this, the unsupervised method presents advantages towards a more global automation of the damage detection process.

To refer that the application of the supervised approach, depending on the direct detection of potential damage reflections in the current sensor signals, requires such reflections to present considerable amplitudes in order to be identified from the remaining noise in the signal (higher SNR). To achieve this, an increased actuation power and/or the enhancement of sensor signals (through the previously referred phased array sensing method) are required. To note that, due to this aspect, this approach will present better results when a phased array based scan/inspection is applied. In the previous development of transducer networks, due to the characteristic individual actuation, it was verified that the application of this method was not possible low SNR with the reflections being less easily directly detected in the sensor signal analysis.

Either in the previous method or on the second one, to present next, to decrease the random influence of noise in sensor signals, as performed for the PZT networks and for the same reasons, each scan was repeated consecutively fifty times (with the wavefront propagating in the same direction). This was performed for each and all scans executed (for the entire component, considering all inspection directions) both for the reference and actual

health conditions, saving all corresponding sensor signals. After performing the multiple repeated scans, sensor signals corresponding to each transducer and for each scan direction are averaged, maximized and minimized for each and all times, as it was performed in the network SHM system. Based in a Gaussian distribution approach new maximums and minimums corresponding to a 90% probability that the signal will be contained in such range, are determined, for all times. Signal bands are then obtained for all sensor signals corresponding to the actual and reference conditions of the component, for all scans, i.e., inspection directions. Specifically for the unsupervised approach, the comparison of sensor signals for current and reference states, for each of the different scans (and for each sensor), is then based on the verification of when the current health state corresponding signal band differs from the reference band by more than 50% of its width.

In the damage detection procedure to be applied, as it was done before, all possible reflections are considered. To further contribute for the reduction of the influence of (random) noise and resulting false indications, the possible damage locations to be determined for each reflection, for each sensor signal and for each inspection scan (for every deployment of the array for the same and different directions of inspection, or directions of propagation of the wavefront) are superimposed being equivalent to perform the intersection of all possible damage locations and forming a damage index. In this manner, it is predicted that the indication of damage positions will be enhanced with relation to false positive since the probability of the intersection of the random false indications resulting from (random) noise to fall in the same position is reduced. In this process bandpass filters are also applied to sensor signals, around the elected frequency for the application of the method (actuation and excited waves and reflections frequency) as before.

The second procedure was derived from the Time of Flight determination of damage reflections considering the excited wavefront and the wave reflection generated by the damage (in this case considered as a curved circular wave propagating and not as a linear wavefront). Please refer to the procedure depicted in Figure 3.

For each transducer in the array and for each scan (inspection direction) the sensed signal (band) is searched for potential damage reflections. In this procedure the ToF determined concurrently by the first method is also used. As referred previously, the ToF of all reflections are considered, in this case until the ToF of the reflection of the farthest boundary (corner) with relation to the phased array is reached since the damage is contained in the component.

Since the signals from the individual sensors are considered in this method,

although the phased actuation is applied, the reflections to be searched for will not be directly enhanced by the phased array sensing method. Since it will be prone to give better results with such expected smaller reflection amplitudes it was considered the application of an unsupervised approach with this method, i.e., considering the comparison/subtraction to a baseline or reference health state corresponding signals (obtained in previous scans and saved), and then determining the outliers.

In this damage detection technique, the known direction of propagation of the wavefront (predetermined by the phase delays) or the predetermined inspection direction is marked for each one of the sensors in the array for the specific scan. All the Time of Flights considered are then related with the corresponding total traveled distance of the activated wavefront and reflected wave, through the known wave propagation velocity. As referred before, a damage distance corresponding to half of the total traveled distance is determined and marked in the inspection direction lines for each and all PZTs Figure 3, corresponding to the intersection point of the line representing the wavefront propagation direction and the line marked as wavefront at t_{max} (in light blue). Departing from each of those initial points and through the Time of Flight, parabolas are determined for each PZT. Each parabola is symmetric with relation to the inspection direction line passing through the corresponding transducer. It has its focus point in the corresponding transducer considered and its directrix parallel to the generated wavefront at a distance from the transducer corresponding to the Time of Flight previously determined considering the known wavefront (wave) propagation velocity. The intersection of all the parabolas will determine (enhancing) the damage location, eliminating (or decreasing the relative importance of) the false indications.

For the same reasons, the same method presented earlier was applied, regarding the generation of an identical mesh and corresponding array. In this array, the point in the first line and first column corresponds to the left corner in the boundary closer to the phased array with the columns representing the points in a direction parallel to the phased array. The same process is then followed regarding now the determined parabolas (instead of circles and ellipses, as before). To decrease the processing time for the calculations performed corresponding to a certain inspection direction/region (to a certain direction of propagation of the generated wavefront) only the points in the mesh in a region delimited by the inspection region (in between, or delimited by the dashed yellow lines in Figure 3) and by the wavefront passing in the initially determined points (wavefront at t_{max} in Figure 3, marked in light blue) are considered. As referred before, the inspection region is determined by the aperture angle of the phased array, centered in the

propagation direction of the corresponding scan. This approach revealed to be still time consuming. A second approach was developed based on the different delays, predetermined, and set to be applied by the actuation system and corresponding propagation directions of the excited wavefronts. For each of such set (inspection) directions, the distance of each point in the mesh to a considered transducer in the phased array is determined and summed to the distance of such mesh point to a line parallel to the excited wavefront, passing by the centre PZT in the array. This value is then introduced in a new array created similarly as the one referred before. This process is repeated with the generation of seven arrays, one for each transducer and each inspection direction. With the known wave propagation velocity each ToF determined (which includes the ToF of the excited wavelength plus the ToF of the potential damage reflection) for all detected potential damage reflections in a sensor signal for a determined inspection direction is translated to a total travelled distance (by the wavefront and potential damage reflection). A range of distances obtained from such total travelled distance, plus or minus $5mm$ (related with mesh spacing) is established. It is then verified if each distance in the array corresponding to such sensor and inspection direction falls in that range for all potential distances and for all sensors and scans (considering that the different directions of inspection were selected to promote a slight superposition of the different corresponding inspection regions). If this condition is verified, a unity value is introduced in the array in the corresponding position and the subsequent process referred for the first approach is then executed with the final determination of the probability of damage existence for each candidate point. This is the approach that was used in the end since it enabled a considerable reduction of processing time.

4.6 Damage Detection: Metallic Plates

The phased array system was then experimentally tested in the $1.5m$ x $1.5m$ x $2mm$ aluminum plate subject to different boundary conditions ranging from totally supported (to increase Lamb waves propagation damping) to simply supported and riveted in the boundaries. The experimental setup is presented in Figure 22. The experiments were conducted first in a laboratory setting and afterwards in an aircraft maintenance hangar with no surrounding noise control and limited temperature control. Experiments were performed with the introduction (cumulatively) of surface and through the thickness circular holes and cuts (with different orientations) with a maximum dimension of 1mm, to simulate damage, as before. Damages were not inflicted around the phased array, respecting the non inspected distance of

$56mm$.

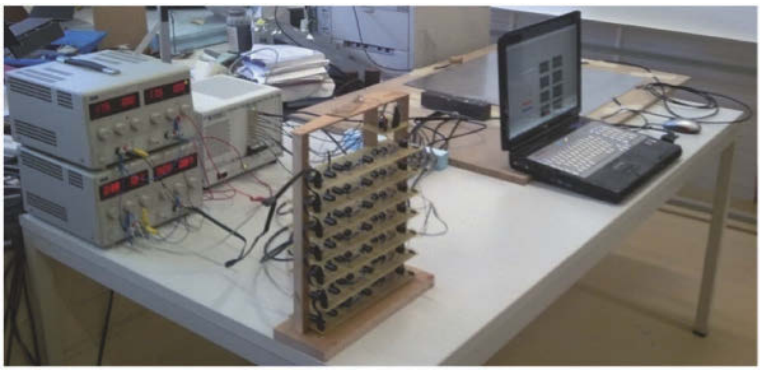

Figure 22. Phased array experimental setup

A total of 46 damages were introduced cumulatively in different positions in the entire aluminum plate. From these, 17 damages were simulated by through the thickness holes, 7 damages by surface holes, 9 damages by surface cuts, 3 oriented in a radial direction considering the center as the phased array, 2 oriented perpendicular to the local radial direction, 1 at 45° from the local radial direction and 3 randomly oriented, at an angle (around 30° and 60°) with the local radial direction and 13 damages by through the thickness cuts, 5 oriented in a radial direction considering the center as the phased array, 2 oriented perpendicular to the local radial direction, 2 at 45° from the local radial direction and 4 randomly oriented, at an angle with the local radial direction).

The simulated damages were successfully detected, even considering damages imposed in the direction of application of the phased array. The only exceptions were damages created behind other damages previously introduced, i.e., in the same radial direction with relation to the phased array (originating in the phased array) and also 60% of the cuts aligned with wavefront propagation directions, since their thickness was inferior to $1mm$.

The software for automated inspection previously developed for networks (in LABVIEW ®with embedded MATLAB ®codes for signal processing and to implement the damage detection algorithms) was adapted for the phased array system. Subsequently the software for networks and the software for phased arrays were integrated as two modules of an inspection software that can be applied for both network and phased array configurations.

A typical results window from the code is shown in Figure 23. In this plot the superimposed solution (tomography based) is presented to the user as the plot of the resultant, final matrix described and obtained through the method explained in the end of the previous section. In this particular case an existing through the thickness circular hole of $0.5mm$ in diameter was enlarged to 1mm in diameter (in the position in the plate presented as dark red in the plot). In these plots the most probable region where damage exists appears in dark red and the lowest probable areas in dark blue, passing by light red, orange, yellow, green and light blue. This result is presented to prove the capability of the system to monitor damage growth (in steps inferior to $1mm$) since the baseline used, i.e., the reference health condition of the plate considered for comparison/subtraction was for an existing damage of $0.5mm$ then enlarged by another $0.5mm$.

In Figure 23, it is also presented the results given by the code obtained from the values of the final matrix representing the six areas with highest probability of damage existence (normalized to one, by the damage index/probability of the most probable area for damage existence). In these results the coordinate system's origin is positioned in the center of the phased array (in the middle of the lower boundary in the figure), with the X axis being parallel to the array direction (pointing to the right side in the figure) and the Y axis being perpendicular to the array (pointing upwards).

In this plot, the remaining colors represent the consideration by the system of false positives due to noise (interfering more, usually, with boundary and other damage reflections) and also due to the intrinsic and inevitable generation of other waves (with smaller amplitude) than the wavefront and corresponding generated reflections in the damage (where mode conversion could also happen). Those additional waves/wavefronts include S_0 wavefronts of smaller amplitude with relation to the main wavefront (being generated and propagating before and after such wavefront, due to the actuation signal morphology) with the same propagation direction and velocity and include also A_0 waves and wavefronts (different mode first antisymmetric Lamb wave mode) propagating with different velocities and then in different directions than the S_0 wavefronts. The existence of other S_0 waves/wavefronts (propagating just before and after the main wavefront) and corresponding damage reflections will be responsible for the determination of different ToFs and then for shifting the determined damage position along the inspection direction. The existing A_0 waves/wavefronts (propagating in different directions and with different propagation velocities) will be responsible for the determination of damage positions in directions apart from the inspection direction.

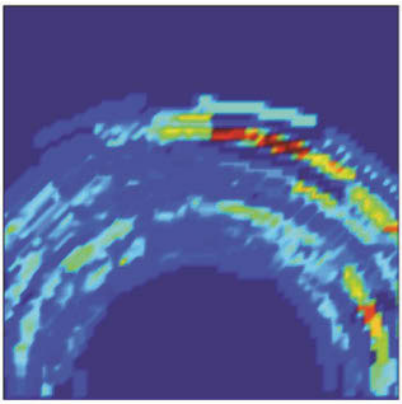

X (m)	Y (m)	Probability
0.26	1.05	1
0.22	1.07	0.82
0.625	0.3	0.6
0.72	0.72	0.55
0.55	0.9	0.5
0.5	0.8	0.45

Figure 23. Damage location contour output

5 SHM using Fiber Optic Sensors

Fiber Bragg Gratings (FBGs) are becoming increasingly more popular for such applications due to their advantages such as their size, immunity to electro magnetic interference, multiplexing potential and absolute reading. FBGs can be used to measure strain and temperature among other properties. Another useful sensor is an etched fiber sensor (EFS). This type of sensor is quite simple; a small section of optical fiber is etched to expose the core. When this etched region is surrounded by resin (fluid) flowing through the mold, the light power that is transmitted through the optical fiber changes hence enabling the sensor to detect fluid (Ahn et al., 1995). Since both EFS and FBG sensors allow light to pass there is potential for them to be multiplexed on one single fiber.

Many researchers have studied the use of a single type of embedded fiber optic sensor however there is less exploration into the use of a combination of sensor types on a single optical fiber. Most of the work that has been done involves the combination of FBG and extrinsic Fabry-Perot interferometer (EFPI) sensors (Kang et al., 2000). EFPI sensors cannot be multiplexed on a single fiber; this severely limits their use when multiple sensors are required. Since ingress/egress issues of fiber optics are not trivial it is highly desirable to minimize the number of instances by placing the largest practical number of sensors on one single fiber. If optical fiber is embedded for the use of sensors in one particular stage of a composite material's life (such as in service) then it is only logical to optimize the use of the fiber and combine sensors that could be used during other stages such as manufacturing.

Here, two FBG sensors and three EFS sensors multiplexed on a single fiber are embedded in a fiberglass panel with a purpose built RTM mold that has a glass viewing window that allows for visual monitoring of the resin injection process. The sensors are monitored during injection to detect the presence of resin and indicate possible dry spots. The viewing window in the mold is used to confirm the sensor readings. Two EFS sensors are also embedded in a semicircular tube to demonstrate their applicability to 3D surfaces such as those found in aerospace applications. The second part of this study involves the use of embedded FBG sensors to detect strain in the composite. Specimens are prepared and tested in a material test machine to determine the strain sensitivity of the FBGs.

To produce composite components with embedded fiber optics a resin transfer moulding laboratory-scale apparatus has been designed and built. The apparatus has the flexibility of accommodating different mold designs and thicknesses, with the feature of a glass viewport to allow for visual monitoring of resin flow during the injection process. It has been tested by producing composite parts with different geometries such as flat panels, hollow and foam cored square and semicircular tubes made from various types of reinforcements. The general layout of the experimental apparatus is shown in Figure 24. The apparatus can be separated into seven separate components: the injection system, injection valve, mold, manipulating/clamping fixture, catchpot, vacuum pump and temperature controller. It can be described as a clamshell system with the mold mounted on it. For a mold to be used with this apparatus it must be $533mm$ X $850mm$. Any thickness is possible with minor modifications to the clamping system.

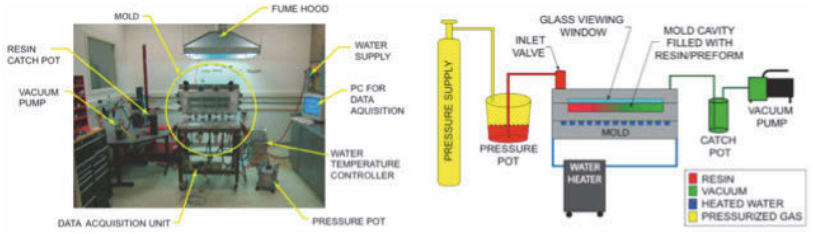

Figure 24. Layout (left) and schematic of RTM apparatus (right)

Fiber optic ingress/egress is one of the most important issues for the application of embedded fiber optic sensors in real composite components (Green and Darvish, 1996) and has been addressed by various researchers (Udd, 1995),(Kang et al., 2000),(Green and Darvish, 1996) however little information on ingress/egress with RTM is available in the literature. The

closed nature of the RTM process as well as the extremely fragile nature of optical fiber makes the ingress/egress of FBG sensors into the mold challenging. Sealing issues also arise due to the extremely small diameter of the optical fiber. When optical fiber is embedded with the in-plane method, the ingress/egress point of the optical fiber is located at the edge of the composite. This eliminates the possibility of trimming the outer edges of the composite to size, a very common practice in the industry. To remove a composite part from a mold it must be removed normal to the mold, therefore the embedded fibers must enter and exit through the mold so that upon removal, the fibers are not severed. A novel through thickness ingress/egress method has been developed, which can overcome the limitations of the in-plane method and be applicable to closed mold processes such as RTM.

A novel method to achieve a through thickness ingress/egress that is applicable to pressurized injection molding such as RTM has been developed. Two major obstacles were overcome when developing this technique, sealing the optical fiber and protecting the fiber as it entered the mold. Optical fiber is quite delicate and must maintain a minimum bend radius before it fractures. When a through thickness fiber ingress technique is used the fiber sees an abrupt 90° bend as it travels through the mold and into the thin composite part as shown in Figure 25 (left). This is inherent to any through thickness ingress/egress technique.

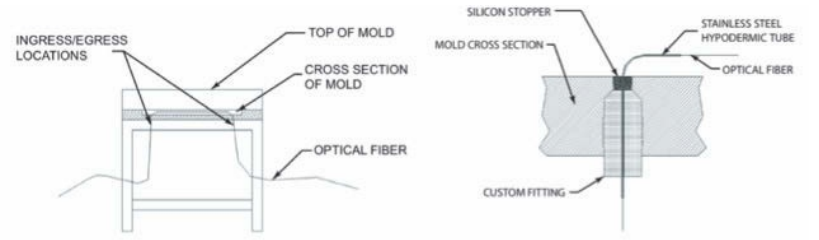

Figure 25. Path of fiber for through thickness ingress/egress (left), and the schematic of fiber sealing (right)

To protect the fiber with minimal disturbance to the composite material a thin hypodermic tube is placed around the fiber. This protects the fiber through the radius of the bend as well as reinforces the fiber at the ingress/egress point once the part is removed from the mold. As one would imagine it is difficult to seal around something as small as an optical fiber that has an outer diameter of 250μm without permanently caulking

or bonding the fiber into the mold. A tapered silicone stopper was used to seal around the hypodermic tube as shown in Figure 25 (right). A custom fitting is used to keep the stopper and fiber in place. Figure 26 shows the panel and semicircular tube with embedded optical fiber.

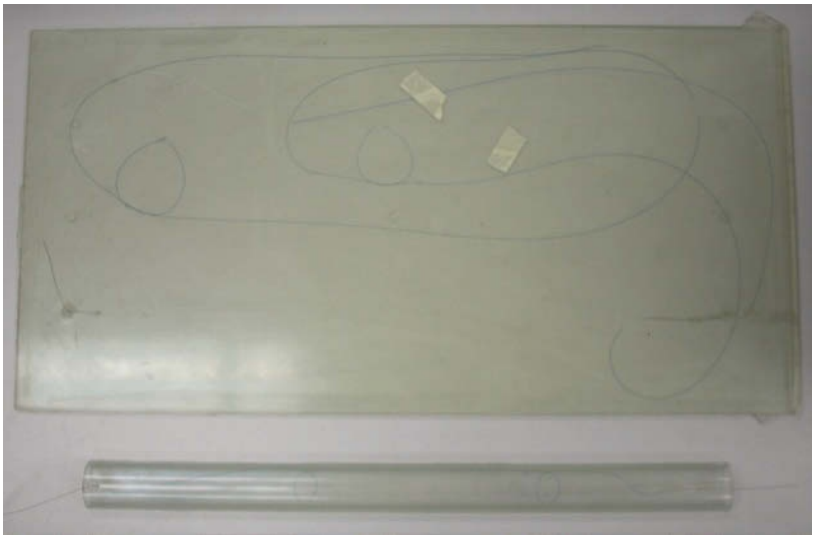

Figure 26. A panel and semicircular tube with embedded optical fiber

The novelty of this technique lies in the use of the tapered silicon stopper and custom fitting. One technique briefly reported by (Kosaka et al., 2003) involves the use of a plastic plug that seals the fiber into the mold and remains bonded to the surface of the composite once it is demolded. The detraction of this technique is that the plastic can become debonded from the composite while in service thereby severing the fiber and rendering the system useless. Also, the fiber must be sealed to the plastic, likely with a caulking that requires time to cure and cannot removed or adjusted if required. The technique developed and described here overcomes these detractions by using a tapered silicon stopper that applies pressure to the hypodermic tube thereby sealing it instantly without any caulking. This allows the fiber to be adjusted at any point prior to injection. Since the stopper is silicon it is easily removed after molding. This technique can be applied to a mold of any thickness over $10mm$ by simply adjusting the length of the fitting. This modularity comes in useful due to the wide variation of RTM molds. The fitting also allows the injection pressure to be

quite high since it is threaded into the mold making this technique applicable to higher-pressure injection techniques such as SRIM and thermoplastic injections.

5.1 Fiber Bragg Grating Sensors

Fiber Bragg Gratings (FBGs) are becoming increasingly more popular for many applications due to their previously stated advantages. They have been used to measure properties such as displacement, strain, temperature, pressure, humidity and radiation dose among others (Dennison and Wild, 2008). FBGs were first demonstrated by (Hill et al., 1978). Embedded FBGs can be used for three distinct purposes during the life of a resin transfer molded part. An array of FBGs in a mold can monitor the mold filling process and can ensure that the mold is completely filled with resin as demonstrated by (Novo et al., 2000). Once injected the resin must go through a specific time-temperature cure cycle. In complicated 3-D parts with varying thicknesses and surface areas, different regions of resin cure at different rates and to varying degrees across the part. FBGs have been used to monitor the cure throughout the part (Kang et al., 2000),(Dewynter-Marty et al., 1998),(Murukeshan et al., 2000),(Jung and Kang, 2007). Once in service the embedded FBGs can be used in a variety of ways to monitor the health of the part thereby reducing maintenance cost and service time while increasing safety (Leng and Asundi, 2003),(Sundaram et al., 2005),(Guo, 2007).

A fiber Bragg grating is a segment of a single mode optical fiber core with a periodically varying refractive index in the axial (longitudinal) direction and commonly created using a high intensity UV laser (Othonos et al., 1999). It allows a broad band of light to pass through while reflecting back a narrow band based on a wavelength known as the Bragg wavelength. The reflected wavelength depends on the grating pitch (spacing between the refractive index variations) and the variation in refractive index. The periodic modulation of the refractive index at the grating location will scatter the light traveling inside the fiber core. Out of phase scattered waves will form destructive interference thereby canceling each other and in phase light waves will add up constructively forming a reflected spectrum with a center wavelength known as the Bragg wavelength.

5.2 Etched Fiber Sensors

Etched fiber sensors are an excellent low cost method of detecting the presence of resin. Operation of etched fiber sensors is quite simple requiring only standard equipment found in most optics lab. Essentially, a light source

launches light into one end of the fiber optic and an optical power meter measures the light intensity at the other end. When resin makes contact with the sensor there is a sudden, sustained drop in the transmitted light intensity (Lim, 2000). The amount of light lost through the etching is a function of the refractive index of the medium it is in (Hect, 2006). This type of sensor has been used to measure the permeability of fiber perform materials by Ahn, S. H. et al (Green and Darvish, 1996) and Lim, S. T. et al (Novo et al., 2000) among others.

The theory behind the etched fiber sensor is very basic; it pertains to the fundamental principles of light transmission through optical fiber. The sensor consists of a small section of optical fiber roughly 3-5mm long with the cladding removed leaving the fiber core exposed. Light is contained in the core of an optical fiber by the cladding. As light travels through the core of a fiber it is continuously bouncing off the cladding. When the light reaches the section of fiber where the cladding is removed a small portion of it escapes while most is transmitted (Eum et al., 2007). When resin contacts the core its refractive index being higher than that of the glass causes more light to escape. Therefore the amount of light transmitted through the fiber is less.

A novel variation of the basic sensor is used in this study. This variation involves looping the etched sensor to create a bend in the etched portion of the fiber. This is done to allow more light to escape from the sensor while leaving some of the cladding on the core to physically protect it. The looped variation is a more robust version of the sensor that is easier to handle and implement. Another benefit of looping the fiber is that the sensitivity can be tuned by adjusting the radius of the loop. As the radius of the loop increases the amount of transmitted light increases. This option is desirable when multiple sensors are used on a single strand of fiber and minimum light loss is desired so that all sensors can make readings. Figure 27 shows the sensor with a Canadian quarter for reference (23.81mm diameter); note the etched section in the upper right portion of the loop.

5.3 Sensor Characterization

To demonstrate the capabilities and multiplexing potential of FBGs and etched fiber sensors, experiments were performed in the aforementioned RTM apparatus using the described ingress/egress technique. The experiments validated the ability of the EFS sensors to detect the presence of resin during the RTM process and the FBG sensors to be used to detect strain all while multiplexed on a single fiber. To explore the versatility and potential for different applications of these sensors three different specimens were pro-

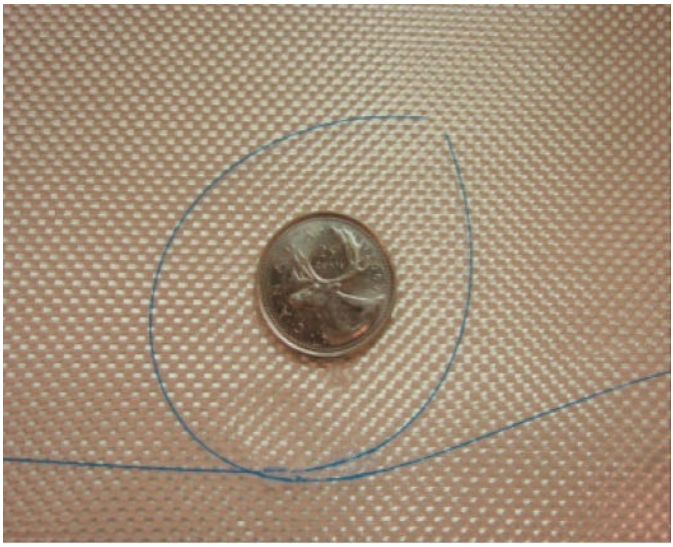

Figure 27. Looped etched fiber sensor

duced; a quasi 2D flat panel and two 3D hollow tubes with a semicircular cross section.

The flat panel was composed of 18 plies of $200gsm$ plain weave glass fiber cloth and Huntsman Renfusion 8601 epoxy resin, with dimensions of $610mm$ X $305mm$ X $3mm$. An optical fiber containing three EFS sensors and two FBG sensors was embedded on the upper ply of the panel.

Two semicircular tube specimens were produced; one composed of five layers and the other composed of six layers of $200gsm$ plain weave glass fiber cloth and Huntsman Renfusion 8601 epoxy resin fully enclosing a steel mandrel that is removed after molding. The tube has an outer radius of $38mm$, length of $500mm$ and wall thickness of $1.5mm$. In the specimen composed of five layers, an optical fiber containing two EFS sensors is embedded between the fourth and fifth ply on the curved surface of the specimen. The specimen composed of six layers contains two FBGs embedded between the fourth and fifth ply on the curved surface of the specimen. The inner layer is considered the first layer in these specimens increasing towards the outside of the tube.

5.4 Flow Monitoring

Flow monitoring experiments were performed during the resin transfer molding process. The general procedure was similar for both specimens and involved embedding the optical fiber in the mold, closing it and injecting the resin. The optical fiber was connected to a photodetector and measurements were logged throughout the injection process.

5.5 Flow Monitoring of Panel Specimen

An optical fiber containing three EFS sensors (EFS#1,2,3) and two FBG sensors (FBG#1,2,3) was embedded into the mold on the upper ply of the laminate, the mold was closed and the resin was injected. Etched fiber sensor readings were recorded with a photodetector and data logger while the FBGs were manually observed with an OSA. A simple circuit was used to interrogate the sensors as shown in Figure 28. A BBS light source is connected to one end of the optical fiber, the fiber runs through the mold, a 50/50 coupler is connected to the other end of the fiber with one branch of the coupler going to the photodiode and the other to an OSA.

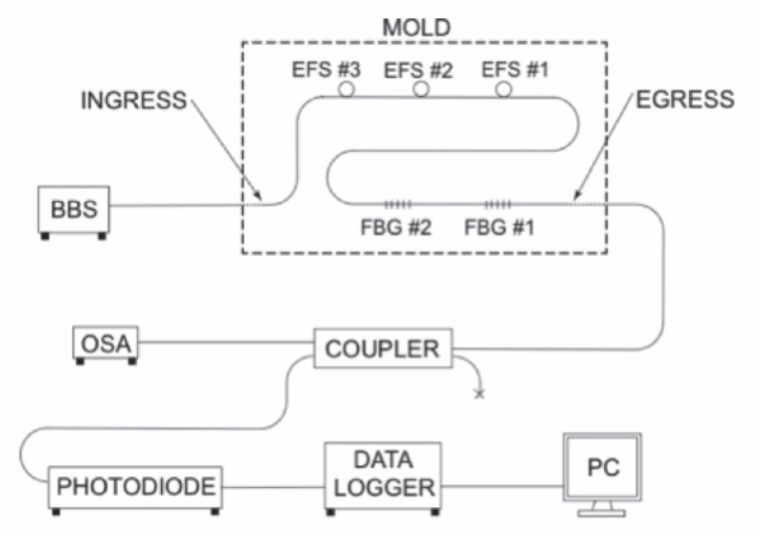

Figure 28. Interrogation system

Figure 29 shows the sensors through the glass viewing window prior to injection. Figure 30a shows the resin approaching EFS #1 while Figure 30b

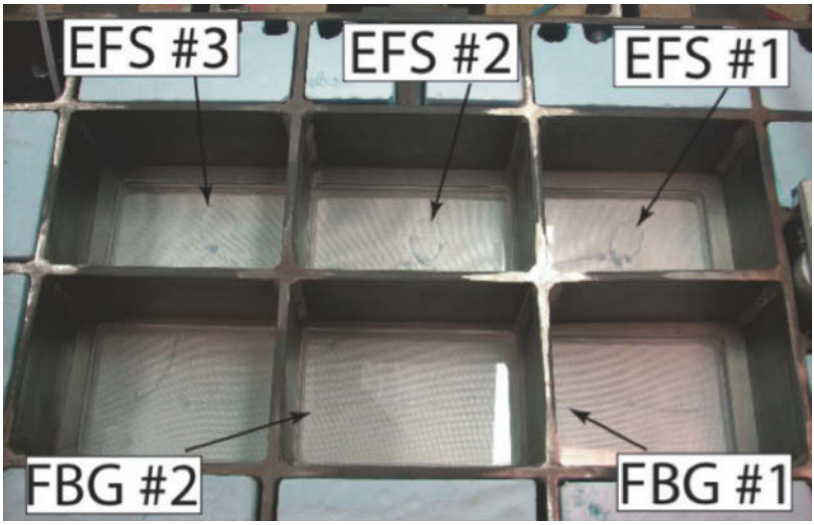

Figure 29. Sensors positioned in RTM prior to injection (mold closed)

shows the resin just after the sensor is saturated and the transmitted light intensity is reduced. This occurs roughly 2.4 minutes into the injection. Figure 30c shows the mold midway through the injection.

Figure 31 shows a plot of the photodiode voltage output vs. injection time. It can clearly be seen that as the resin reaches the first sensor at roughly 2.4 minutes there is a sharp and sustained drop in the transmitted light. Another drop occurs at roughly 7.7 minutes when the resin reaches the second sensor and again at 12.2 minutes when the resin reaches the third sensor. Once the mold was saturated and the injection was complete, the light source was turned off to ensure that the readings could be differentiated from a change in minimal transmitted light and no transmitted light. When the light source was off the photodiode output was zero. The light source was turned back on and the transmitted light intensity was the same as before it was turned off therefore indicating that light was indeed being transmitted. During this time the FBG sensors were manually observed with the OSA to ensure that they were still functional. Due to the arrangement of the sensors on the fiber (FBG before EFS) no change in power was noticed when resin contacted the EFS sensors therefore demonstrating that the EFS do not effect the FBG sensors as long as they are situated after the FBGs on the fiber. The FBG output is not included here however this technique has been thoroughly researched by others such as (Novo et al.,

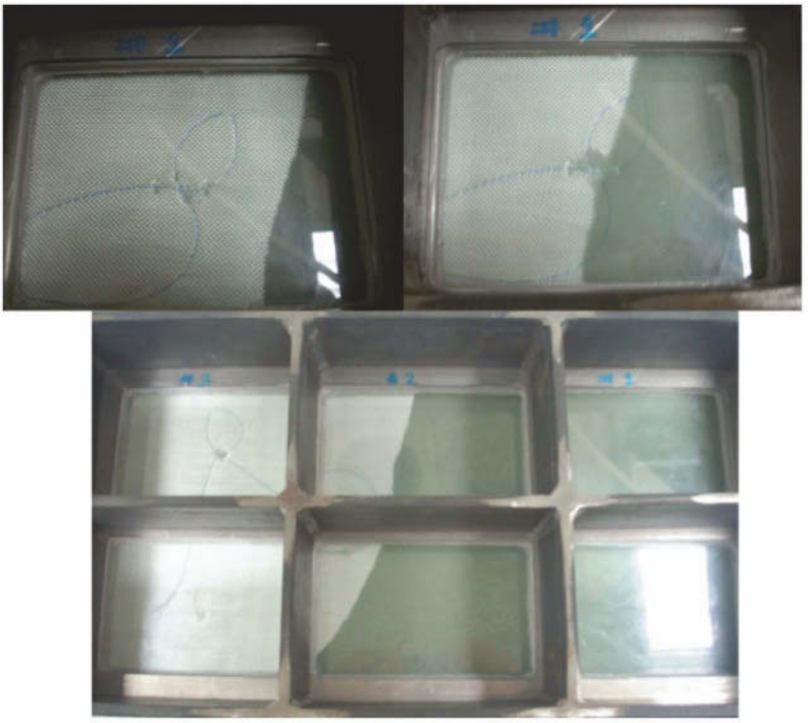

Figure 30. CW from top left: a) resin approaching sensor, b) resin just after contacting sensor, c) mold midway through injection

2000) and (Eum et al., 2007),(Eum et al., 2008).

5.6 Flow Monitoring of 3D Semicircle Specimen

To demonstrate the versatility and applicability of these sensors to more realistic structures, an optical fiber containing two EFS sensors was embedded in a hollow tube with a 3D semicircle cross section using the aforementioned RTM apparatus. The sensors were embedded between the fourth and fifth layers on the curved surface of the semicircle. The flat side of the semicircle is visible through the viewing window however the curved surface is not. Due to the relatively small radius of the tube and uniform resin flow it can be estimated with a high level of confidence that the resin is in contact with the sensors and their output can be verified. This is a more realistic experiment for these sensors since the majority of industrial molds

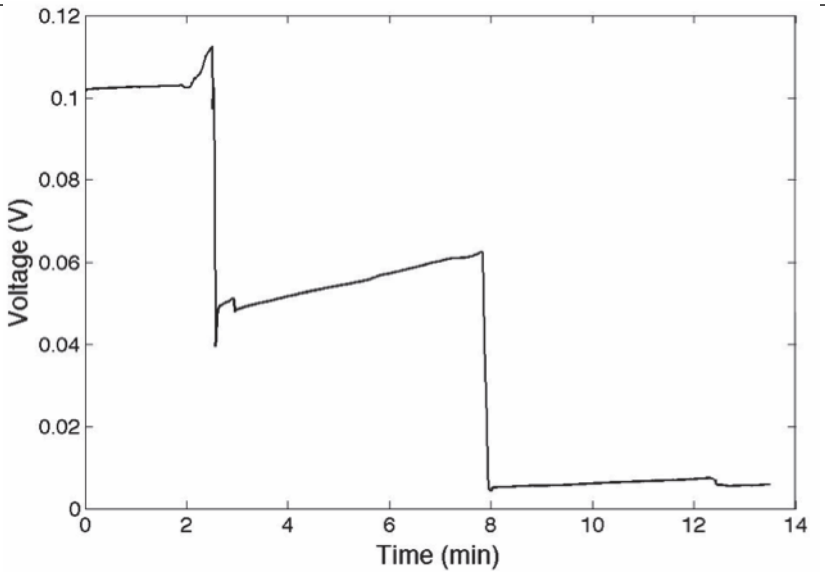

Figure 31. Plot of photodiode output vs. injection time for panel

are not translucent.

Figure 32. Semicircular tube with embedded fiber optic sensors

The sensors were interrogated in a manner similar to that shown in Figure 28. Figure 32 shows the specimen with the sensors visible. Data was recorded during the injection and is shown in Figure 33 showing resin arrival at the first and second EFS at roughly 2.9 and 4.0 minutes respectively.

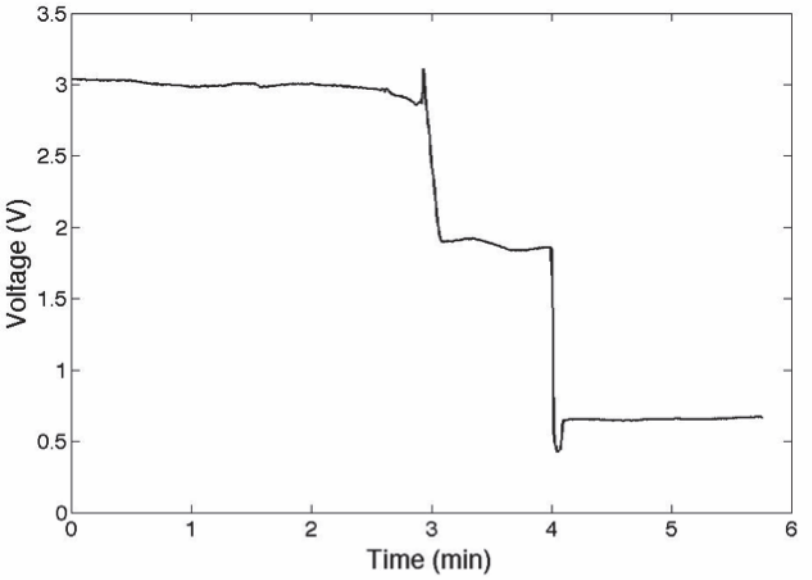

Figure 33. Plot of photodiode output vs. injection time for tube

5.7 Strain Sensitivity Characterization

For FBGs to be used as strain sensors after they are embedded in a composite material the relationship between the shift in the Bragg wavelength and the axial strain in the sensor must be known. This relationship is known as the sensitivity or the strain gage factor, S. Embedded FBG strain gages experience additional radial strain field in application, therefore once integrated into a structure, every gage must be recalibrated (Fan and Kahrizi, 2005).

The strain gage factor for an electrical foil strain gage can be described as the relationship between the resistance of the wire, R, axial strain εa and the change in resistivity of the wire (Wheeler and Ganji, 2004). The expression for the strain gage factor is given in (31).

$$S = \frac{dR/R}{\varepsilon_a} \tag{31}$$

For an FBG, the gage factor would be the relationship between the change in the Bragg wavelength and axial strain. The expression for this is shown in (32).

$$S = \frac{\delta\lambda_B}{\varepsilon_a} \tag{32}$$

To determine the gage factor for both 2- and 3-D specimens they were tested in an MTS 810 material test machine. A 6mm grid, 120Ω strain gage from Omega Engineering Inc. was bonded to the surface directly beside the FBG. The strain gage was connected to a Measurements Group Instrument Division P-3500 strain indicator and the FBG was hooked up to an Ando AQ6331 OSA, JDS Uniphase broadband light source and a 50:50 optical coupler. Figure 34 shows the 2D specimen in the MTS machine with the instrumentation equipment (left) and a close up of the 3D specimen (right).

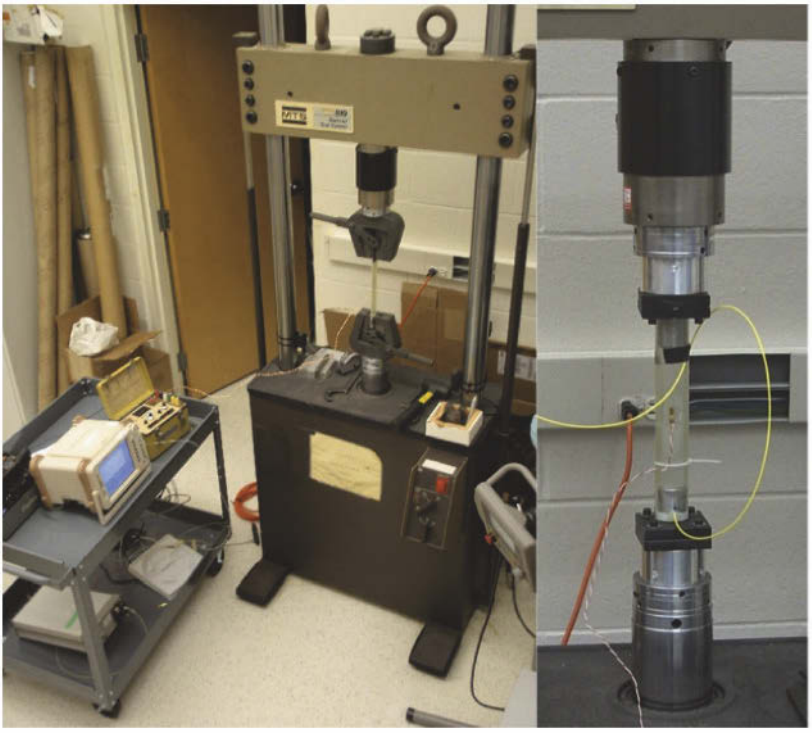

Figure 34. 2D specimen in MTS machine with instrumentation equipment (left) and 3D specimen loaded in MTS machine (right)

5.8 Strain Sensitivity of Panel Specimen

To determine the gage factor for the panel a tensile specimen was cut out of the RTM'd panel. The specimen has dimensions of $38.1mm$ X $300mm$ X $3mm$. The embedded FBG is located directly in the middle of the specimen along the length and width. Small pieces of sand paper were bonded to the ends of the specimen to help the test machine grip without slipping.

The specimen was loaded into the test machine and a tensile load was applied at a rate of $0.051mm/min$ up to a maximum of roughly $2.88mm$. Readings were taken at roughly $0.254mm$ intervals starting at zero strain. The test was repeated four times to ensure the repeatability of the results. Figure 35 shows a plot of the collected data, namely, Bragg wavelength vs. measured strain.

A linear line was fit to the data with an equation of $y = 0.001141x + 1541.04$ with an R^2 value of 0.999 obtained from four test runs. ¿From this equation we can ascertain that $S = 1.141 \times 10^{-3}$ or every $1.141pm$ shift in the Bragg wavelength is equal to one micro strain.

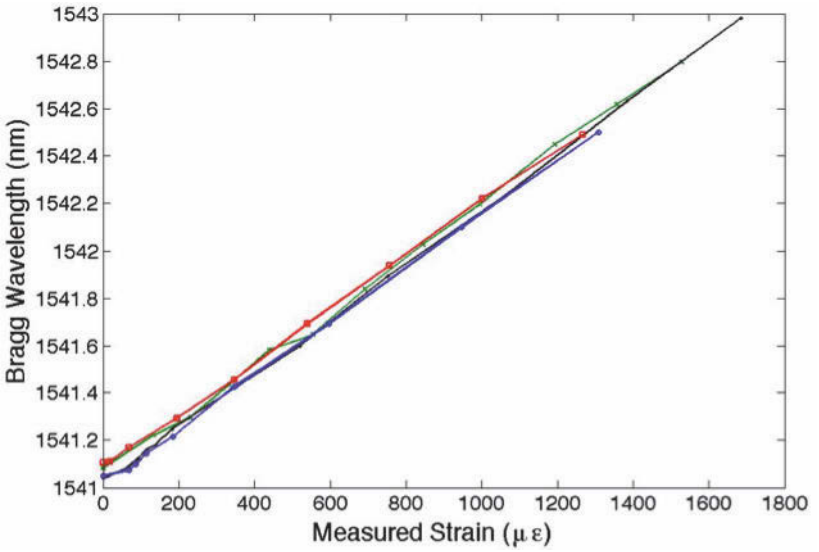

Figure 35. Bragg wavelength vs. strain gage measured strain for 2D panel

5.9 Strain Sensitivity of Semicircular Specimen

To determine the gage factor for the semicircular tube a special fixture was designed to restrain the specimen in the aforementioned MTS machine for compression testing. Semicircular blocks, $38mm$ long with the same cross sectional dimensions as the mandrel were fastened to adapter plates that interface with the test machine. The tube was cut at it's mid-length to produce two specimens and simplify the testing process. Each specimen has one FBG at the midspan.

The specimen was slid onto the fixture and a compression load was applied then released. This was repeated twice to ensure repeatability. The strain gage output (in microstrain) and Bragg wavelength (in nm) was recorded as the load was applied and released. The recorded data is plotted and shown in Figure 36.

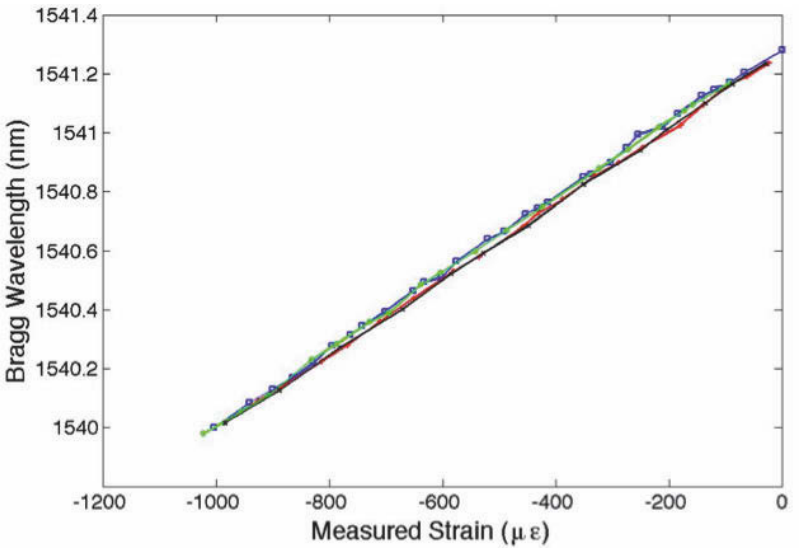

Figure 36. Bragg wavelength vs. strain gage measured strain for 3D structure

A linear line was fit to the data and an equation of $y = 0.001288x + 1541.28$ with an R^2 value of 0.999 was obtained from four test runs (two loading, two unloading). From this equation we can ascertain that $S = 1.288e - 3$ or every $1.288pm$ shift in the Bragg wavelength is equal to one micro strain.

As mentioned earlier the strain sensitivity of the embedded FBG is

$1.141pm/\mu\varepsilon$ for the flat panel specimen and $1.288pm/\mu\varepsilon$ for the semicircular specimen. These sensitivities deviate from the commonly referenced value of $1.2pm/\mu\varepsilon$ (Othonos et al., 1999) for a bare FBG with typical material properties by -4.9% and 7.3% for flat panel and semicircular specimens respectively. These values fall within the range of deviation reported by Fan, Y., et al (Fan and Kahrizi, 2005). Factors such as variations in the material and manufacture of each individual FBG and experimental error in the processing and testing phase such as misalignment of FBG or strain gage with the axis of the specimen may contribute to this deviation. Another factor which may contribute to the variation in sensitivity between the two geometries is the mismatch of mechanical properties between the FBG fiber and host structure, particularly their Poisson ratio in the lateral direction as embedded sensors experience an additional radial strain field when load is applied along the sensor direction (Fan and Kahrizi, 2005).

6 Concluding Remarks

Piezo transducer network and linear phased array SHM systems have been developed for damage detection and location in metallic and composite plate structures. The SHM systems were based on the first symmetric mode (S_0) of Lamb waves. The most important advantages and simultaneously the main difficulties in the application of the S_0 mode that were overcome here are related to its high propagation velocity. The advantages are that, with the application of this wave mode and its high propagation velocity, this wave and its reflection suffer a small interference from lower propagating waves (modes). Furthermore, due to their deformation pattern they are more prone to detect any types of damage in the components, being easier to deal with, while presenting small amplitude propagation damping. Regarding obstacles that were overcome, due to such high propagation velocity, difficulties emerge in the generation of wavefronts resulting from the constructive interference of waves generated by the single actuators in the phased array and particularly in the precise establishment of the small time delays required for the phased actuation. One other difficulty is related with the small amplitude of damage reflected waves. This negative aspect is diminished by the use of the phased array and beamforming, increasing the amplitude of actuation and then the amplitude and SNR of reflections. Furthermore, with the application of a phased array, an entire component can be inspected by performing several scans in which the inspection direction is defined and changed from scan to scan. In this manner the inspection region is delimited for each scan, resulting in an intensification of inspection effort in such a region, decreasing simultaneously the complexity and

increasing the precision of the inspection process. Also in the actuation of Lamb waves, their dispersive behaviour, i.e., the dependency of their propagation velocity to their frequency, must be accounted for. This means that the actuation signal waveform must excite one single frequency, to obtain a wave with a particular frequency, propagating with a unique velocity.

A dedicated actuation system, required for the phased generation of the waves and wavefront was developed. This system is based on a master MCU circuit, controlling the phased activation of slave channels. The master MCU has programmed the time delays to be applied for the phased activation for each and all scan (directions) to be implemented. Furthermore, in that code the number of scans and scan repetitions are also determined. The slave circuits/channels, connected to each PZT in the array, generate the correct actuation signal waveform. In these circuits, an output switch was applied to match the impedance of actuation and acquisition systems, what is a usual problem in the current existing systems. With the use of such switch, measured wave amplitudes were increased significantly.

Bibliography

S. H. Ahn, W. I. Lee, and G. S. Springer. Measurement of the Three-Dimensional Permeability of Fiber Preforms Using Embedded Fiber Optic Sensors. *Journal of Composite Materials*, 29(6):714–733, April 1995.

C. R. Dennison and P. M. Wild. Enhanced sensitivity of an in-fibre Bragg grating pressure sensor achieved through fibre diameter reduction. *Measurement Science and Technology*, 19(12):125301, October 2008.

V. Dewynter-Marty, P. Ferdinand, E. Bocherens, R. Carbone, H. Beranger, S. Bourasseau, M. Dupont, and D. Balageas. Embedded fiber Bragg grating sensors for industrial composite cure monitoring. *Journal of Intelligent Material Systems and Structures*, 9(10):785–787, 1998.

USA Department of Defense DOD. Airplane damage tolerance requirements. *MIL-A-83444, Washington DC, USA*, 1987.

S. Eum, K. Kageyama, H. Murayama, I. Ohsawa, K. Uzawa, M. Kanai, and H. Igawa. Process/health monitoring of turbine blades with FBG sensors with multiplexing techniques. *Proceedings of SPIE*, 7004, June 2008.

S. K. Eum, K. Kageyama, H. Murayama, I. Ohsawa, K. Uzawa, M. Kanai, and H. Igawa. Resin flow monitoring in vacuum-assisted resin transfer molding using optical fiber distributed sensor. In *Behavior and Mechanics of Multifunctional and Composite Materials 2007*, pages 65262T–65262T–8. SPIE, April 2007.

Y. Fan and M. Kahrizi. Characterization of a FBG strain gage array embedded in composite structure. *Sensors and Actuators a-Physical*, 121 (2):297–305, June 2005.

V. Giurgiutiu. *Structural health monitoring with piezoelectric wafer active sensors*. Elsevier Academic Press, Boston, USA, 2008.

A. K. Green and S. Darvish. Practical terminations for optical fibres embedded in composite materials. In *Proceedings of SPIE*, 1996.

Z. S. Guo. Strain and temperature monitoring of asymmetric composite laminate using FBG hybrid sensors. *Structural Health Monitoring*, 6(3): 191–197, 2007.

J. Hect. Understanding fiber optics. *Pearson Education Inc., Upper Saddle River, New Jersey*, 2006.

K. O. Hill, Y. FujiiI, D. C. Johnson, and B. S. Kawasaki. Photosensitivity in Optical Fiber Waveguides - Application to Reflection Filter Fabrication. *Applied Physics Letters*, 32(10):647–649, 1978.

K Jung and T. J. Kang. Cure monitoring and internal strain measurement of 3-D hybrid braided composites using fiber Bragg grating sensor. *Journal of Composite Materials*, 41(12):1499–1519, June 2007.

H. K. Kang, J. W. Park, and C. Y. Ryu. Development of fibre optic ingress/egress methods for smart composite structures. *Smart Materials and Structures*, 9:149–156, 2000.

T. Kosaka, K. Osaka, S. Nakakita, and T. Fukuda. Fiber optic strain monitoring of textile gfrp during rtm molding and fatigue test by using embedded fbg sensors. *Proceedings of SPIE*, 5056, 2003.

J. Leng and A. Asundi. Structural health monitoring of smart composite materials by using EFPI and FBG sensors. *Sensors and Actuators a-Physical*, 103(3):330–340, 2003.

S. T. Lim. An analysis of the three-dimensional resin-transfer mold filling process. *Composites Science and Technology*, 2000.

V. M. Murukeshan, P. Y. Chan, and L.S. Ong. Cure monitoring of smart composites using fiber Bragg grating based embedded sensors. *Sensors and Actuators a-Physical*, 79:153–161, 2000.

C. Novo, O. Frazão, A. N. Costa, A. Vieira, N. Correia, I. Dias, F. M. Araujo, and A T Marques. Progression monitoring of the flow front in RTM process using fibre Bragg grating sensors. *Society of Photo-Optical Instrumentation Engineers (SPIE) Conference Series*, 4185:808–811, 2000.

A Othonos, K Kalli, and G. E. Kohnke. *Fiber Bragg Gratings: Fundamentals and Applications in Telecommunications and Sensing*. Artech House Inc., Boston, Massachusetts, 1999.

R. Sundaram, G. M. Kamath, and N. Gupta. Structural health monitoring of co-cured composite structures using FBG sensors. In *Proceedings of SPIE*, 2005.

E Udd. *Fiber optic smart structures*. John Wiley & Sons, Inc., New York, 1995.

A. J. Wheeler and A. R. Ganji. Introduction to engineering experimentation. Pearson/Prentice Hall Inc., Upper Saddle River, New Jersey, 2004.